

A Bayesian algorithm for the retrieval of liquid water cloud properties from microwave radiometer and millimeter radar data

Sally A. McFarlane and K. Franklin Evans

Program in Atmospheric and Oceanic Sciences, University of Colorado at Boulder, Boulder, Colorado, USA

Andrew S. Ackerman

NASA Ames Research Center, Moffett Field, California, USA

Received 3 July 2001; revised 2 January 2002; accepted 2 January 2002; published 31 August 2002.

[1] We present a new algorithm for retrieving optical depth and liquid water content and effective radius profiles of nonprecipitating liquid water clouds using millimeter wavelength radar reflectivity and dual-channel microwave brightness temperatures. The algorithm is based on Bayes' theorem of conditional probability and combines prior information on cloud microphysics with the remote sensing observations. Prior probability distribution functions for liquid water clouds were derived from the second, third, and sixth moments of droplet size distributions measured by in situ aircraft probes in shallow tropical cumuli. The algorithm also calculates error bars for each retrieved parameter. To assess the algorithm, we perform retrieval simulations using radar reflectivity and brightness temperatures simulated from tropical cumulus fields calculated by a large eddy simulation model with explicit microphysics. These retrieval simulations show that the Bayesian algorithm has similar magnitude errors to current retrieval methods for liquid water content and liquid water path retrievals but has much smaller errors for effective radius and optical depth. We also perform retrievals on three months of data from the Atmospheric Radiation Measurement (ARM) Program's site on Nauru in the tropical west Pacific. For nonprecipitating liquid water clouds over Nauru during June–August 1999 we retrieve a mean optical depth of 9.2, mean liquid water content of 0.112 g/m^3 , and mean effective radius of $7.8 \text{ }\mu\text{m}$. The Bayesian method is a flexible approach to cloud profile remote sensing and could be expanded to other sites or cloud types.

INDEX TERMS:

3360 Meteorology and Atmospheric Dynamics: Remote sensing; 0320 Atmospheric Composition and Structure: Cloud physics and chemistry; 3394 Meteorology and Atmospheric Dynamics: Instruments and techniques; 3399 Meteorology and Atmospheric Dynamics: General or miscellaneous; KEYWORDS: remote sensing, clouds, radar, microwave radiometer, Bayes

1. Introduction

[2] Liquid water boundary layer clouds are an important element of the Earth's radiation budget. Due to their relatively high albedos they can greatly reduce incoming solar radiation, thereby cooling the surface. However, they also exert a warming influence in the thermal infrared over what would exist in a clear sky due to their emission of infrared radiation at fairly high temperatures. To accurately quantify the radiative effects of these clouds on the surface energy budget, information is needed about the horizontal and vertical distribution of their microphysical properties, such as liquid water content and effective radius. Most current data on cloud microphysical properties come from in situ aircraft measurements during field programs. While such data are useful for case studies and statistical databases [e.g., Miles *et al.*, 2000], they have limited temporal and

spatial coverage and are expensive to obtain. To develop long-term data sets of cloud microphysical properties for many different cloud regimes, a remote sensing based retrieval method is needed. One of the objectives of the Department of Energy's Atmospheric Radiation Measurement (ARM) Program is to develop such data sets in order to assess and improve current cloud parameterizations in models.

[3] Microphysical radiative properties of clouds are functions of the cloud droplet size distribution (DSD). The liquid water content (LWC) is proportional to the third moment of the DSD, while extinction is proportional to the second moment, and effective radius (r_e) is the ratio of the third moment to the second moment. Remote sensing instruments cannot directly measure the DSD, as can in situ probes on aircraft. However, they can measure parameters that are related to the moments of the size distribution. Then radiative properties can be retrieved by relating the measured parameters to the desired moments of the DSD.

[4] For radars operating at millimeter wavelengths, cloud droplets are much smaller than the radar wavelength so the Rayleigh approximation applies and radar reflectivity is proportional to the sixth moment of the droplet size distribution. Advances in instrumentation within the last 5 years have led to the development of unattended millimeter wavelength cloud radars with the vertical resolution (~ 45 m) and sensitivity (-60 dBZ) required to study boundary layer clouds [Moran *et al.*, 1998; Clothiaux *et al.*, 1999]. Several algorithms have been developed that seek to relate measured radar reflectivity to liquid water content. These are generally linear regression equations in which the coefficients are determined either from in situ aircraft data [e.g., Fox and Illingworth, 1997] or from cloud models [e.g., Liao and Sassen, 1994].

[5] Moments of the DSD other than the sixth cannot be directly retrieved from remote sensing measurements. However, the total column liquid water path, or vertical integral of the third moment, can be retrieved from a passive dual-channel microwave radiometer, in which one channel is more sensitive to integrated water vapor and the other to integrated liquid water [Westwater, 1978]. The inclusion of total liquid water path adds an additional constraint on the DSD, but is still not enough to describe it completely, so other information or assumptions must be included.

[6] Several combined radar/radiometer retrieval methods have been developed in recent years for stratus and stratocumulus clouds. One of the common assumptions in these retrieval methods is that the droplet distribution can be modeled by a single mode gamma or lognormal distribution with number concentration constant with height and a fixed value of the width of the lognormal distribution, σ_{\log} , or shape of the gamma distribution, ν_{gam} [Frisch *et al.*, 1995; Dong *et al.*, 1997]. Assuming a single mode lognormal distribution with a fixed width and number concentration constant with height is equivalent to assuming that the liquid water content is proportional to the square root of the radar reflectivity [e.g., Frisch *et al.*, 1995, equation (18)]. Miles *et al.* [2000] reviewed a large number of in situ aircraft measurements of stratus clouds and found large variations in σ_{\log} and ν_{gam} . They showed that using climatological values of σ_{\log} can lead to errors of up to 25–75% in some retrieved parameters. Other retrieval algorithms [Dong *et al.*, 1997; Mace and Sassen, 2000] are also constrained to match the downwelling solar flux at the surface, which improves the optical depth accuracy, but does not allow independent validation of the cloud retrievals using solar radiative transfer models, and restricts the retrievals to uniform overcast cloud layers. There has been little research reported on microphysical retrievals from radar and microwave radiometer data in cumulus clouds.

[7] We present a new liquid cloud retrieval method based on Bayes' theorem of conditional probability, which combines remote sensing measurements with prior information on cloud microphysics. We make no assumptions about the shape of the droplet size distribution, but instead use information from in situ measurements about the second, third, and sixth moments of the droplet size distributions. Inputs to the algorithm are cloud location from cloud radar and lidar, profiles of radar reflectivity, brightness temperatures from a microwave radiometer, and radiosonde profiles of temperature and humidity. These data are readily

available from instruments located at the Atmospheric Radiation Measurement (ARM) Program's sites. Outputs of the algorithm are vertical profiles of liquid water content and effective radius, total column precipitable water vapor, liquid water path, optical depth, and uncertainty estimates on all retrieved quantities. Due to the current difficulties in discriminating hydrometeor reflectivities from those caused by insects at the ARM Southern Great Plains (SGP) site in Oklahoma, we are concentrating on marine tropical cumulus data from the ARM Tropical Western Pacific (TWP) site on the Republic of Nauru.

[8] Section 2 describes Bayes' theorem and the justification for basing a retrieval algorithm on it. Section 3 describes the inputs to the algorithm. Section 4 discusses the retrieval algorithm in detail. Section 5 presents a test of the algorithm using data from an LES model while section 6 illustrates results from actual data at Nauru. Section 7 presents a summary of the retrieval and conclusions.

2. Bayes' Theorem

[9] Bayesian theory is a general approach to solving inverse problems such as retrieving a vertical profile of cloud properties from a set of remote sensing observations [Sivia, 1996; Rodgers, 2000]. Following Rodgers [2000], we define the measurement vector, \mathbf{y} , as the set of remote sensing observations (microwave brightness temperatures and vertical profiles of radar reflectivity), each with an associated measurement error. We define the state vector, \mathbf{x} , as the set of all cloud and atmospheric parameters which affect the measurement vector. The basis of Bayesian theory is that the inverse problem can be related to the forward problem through a set of measurements and prior knowledge about the probability of the state vector.

[10] Bayes' theorem of conditional probability is given by

$$p_{\text{post}}(\mathbf{x}|\mathbf{y}) = \frac{p_{\text{f}}(\mathbf{y}|\mathbf{x})p_{\text{pr}}(\mathbf{x})}{\int p_{\text{f}}(\mathbf{y}|\mathbf{x})p_{\text{pr}}(\mathbf{x})d\mathbf{x}}, \quad (1)$$

where \mathbf{x} and \mathbf{y} are the state vector and measurement vector defined above. In this equation, the quantity $p_{\text{pr}}(\mathbf{x})$, is known as the prior probability density function (pdf) of the state \mathbf{x} . It represents our knowledge about the possible values of \mathbf{x} before the measurement is made.

[11] As discussed in section 3.2, we use in situ observations of cloud drop size distributions from aircraft to create a prior pdf. The term, $p_{\text{f}}(\mathbf{y}|\mathbf{x})$, is the conditional, or forward, probability of the remote sensing observations, \mathbf{y} , given the state vector. It is represented by a forward model, which expresses our understanding of the physics that relate the atmospheric and cloud properties to the measured quantities (brightness temperatures and radar reflectivity), including the uncertainties. The forward probability can be modeled as a distribution of observations around a simulated observation, with the width of the distribution given by the measurement and model uncertainties. The denominator simply normalizes the integral. Finally, the term $p_{\text{post}}(\mathbf{x}|\mathbf{y})$ is known as the posterior pdf and is the probability distribution of the state vector given the measurement vector. The posterior pdf is the result of applying Bayes' theorem to a set of measurements and prior information. It

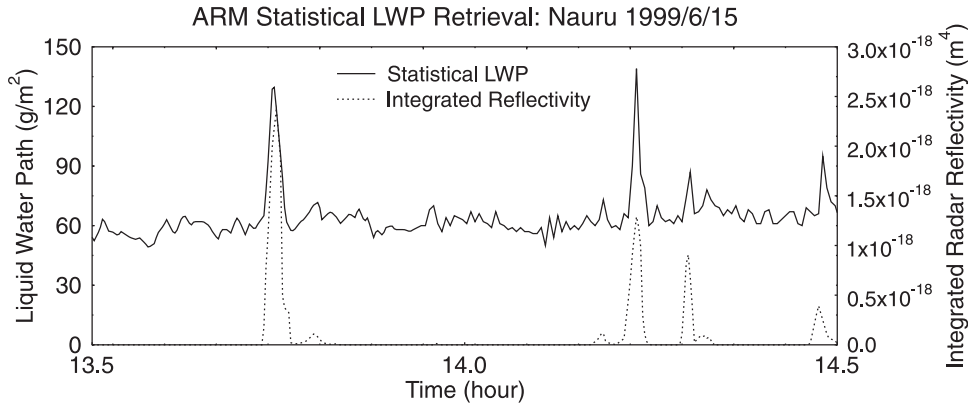


Figure 1. Statistical liquid water path retrieval from MWR and vertically integrated radar reflectivity. At times when there are no radar returns, the retrieved liquid water path has an offset of 30–60 g/m².

represents our knowledge of the cloud properties after the measurements are taken, and includes information from the measurements and the prior pdf.

[12] The application of Bayes' theorem produces a probability distribution of cloud properties. To retrieve a vector of cloud properties, we integrate over this posterior pdf to calculate the mean value,

$$\langle \mathbf{x} \rangle = \frac{\int \mathbf{x} p_{\text{f}}(\mathbf{y}|\mathbf{x}) p_{\text{pr}}(\mathbf{x}) d\mathbf{x}}{\int p_{\text{f}}(\mathbf{y}|\mathbf{x}) p_{\text{pr}}(\mathbf{x}) d\mathbf{x}}. \quad (2)$$

An estimate of the uncertainty in the retrieval is the variance around this mean vector, which is the second moment of the posterior pdf,

$$\sigma_{\mathbf{x}}^2 = \frac{\int (\mathbf{x} - \langle \mathbf{x} \rangle)^2 p_{\text{f}}(\mathbf{y}|\mathbf{x}) p_{\text{pr}}(\mathbf{x}) d\mathbf{x}}{\int p_{\text{f}}(\mathbf{y}|\mathbf{x}) p_{\text{pr}}(\mathbf{x}) d\mathbf{x}}. \quad (3)$$

The computation of these integrals is performed via Monte Carlo integration and is discussed in detail in section 4.

[13] Bayes' theorem is a useful framework for a retrieval algorithm because it relates the inverse problem to the simpler forward problem, produces uncertainties on retrieved variables, and introduces a priori information in a well defined formalism. Since the retrieval of cloud microphysical properties from remote sensing measurements is an ill constrained problem, a priori information is always included in retrieval algorithms, even if not explicitly stated as such. A priori information is necessary to provide a connection between the observed radar reflectivity and liquid water path and the desired quantities of liquid water content, extinction, and effective radius. In a linear regression algorithm, such as $\text{LWC} = aZ^b$, the a priori information is the functional form of the equation and the slope, a , and the exponent, b , which are determined from in situ data or cloud models. In a combined radar/radiometer algorithm the a priori information is the assumed form and width of the DSD, and the assumption that number concentration is constant with height. In both of these algorithms, the relationship between LWC (or effective radius) and radar reflectivity is fixed, based on the particular assumptions made. In the Bayesian algorithm, the prior pdf allows a distribution of relationships between reflectivity and LWC or r_e . For each observed reflectivity there is a

range of possible retrieved LWC and r_e , with some being more probable than others.

[14] The prior pdf must encompass the possible regions of parameter space expected for a particular cloud type since properties outside the bounds of the prior cannot be retrieved. However, the prior should not be so broad that valid knowledge of cloud microphysics is ignored, which would lead to poor retrievals. To expand the Bayesian algorithm to different cloud types or regions, pdfs representative of the given cloud regime must be developed. If little is known of a particular cloud type, then a suitably broad pdf should be chosen.

3. Inputs to Algorithm

3.1. Remote Sensing Observations

[15] The algorithm has been developed for the suite of instruments present at each ARM site, which include a Belfort or Vaisala Ceilometer (CEIL), a Micropulse Lidar (MPL), a Millimeter Wavelength Cloud Radar (MMCR), a Microwave Radiometer (MWR), and Vaisala radiosondes (RAOB). The data from all of these instruments is readily available from the ARM archive (<http://www.archive.arm.gov/>).

[16] The MMCR is a vertically pointing Doppler radar that operates at 34.86 GHz (8.6 mm) [Moran *et al.*, 1997]. It cycles through four different operational modes, each with different sensitivity, spatial and temporal resolution, and aliasing characteristics. Details of the operational parameters of the MMCR at each ARM site are given by Clothiaux *et al.* [1999]. The Active Remote Sensing of Clouds (ARSCL) product described by Clothiaux *et al.* [2000] combines information from all modes of the MMCR with MPL and CEIL data to produce a best estimate of cloud boundaries, hydrometeor reflectivities and vertical velocities at 10 s temporal and 45 m vertical resolution. The ARSCL product is freely available from the ARM archive.

[17] The MWR is a dual-channel radiometer operating at wavelengths of 23.8 GHz and 31.4 GHz. The ARM liquid water path (LWP) retrievals from the MWR are calculated using a statistical linear regression with climatological coefficients (<http://www.arm.gov/docs/instruments/static/mwr.html>). At Nauru, the retrieved LWP is often greater than 40 g/m² at times when the cloud radar reports clear sky. Figure 1 is a plot of the statistical LWP retrieved from

the MWR and vertically integrated reflectivity from the MMCR, showing this offset. This LWP offset is a systematic error due to the use of climatological coefficients in the regression equation, and is expected to affect the cloudy sky liquid water path retrievals as well [Liljegren, 1999]. Therefore we use the brightness temperatures from the MWR, which are the actual observables, instead of the ARM statistical LWP retrievals. The MWR instruments are calibrated by an automated tipping curve calibration, which can provide absolute accuracy of about 0.5 K if performed correctly [Han and Westwater, 2000]. Westwater *et al.* [2000] showed that the MWR was well calibrated during the Nauru99 field experiment (15 June 1999 to 15 July 1999) with the accuracy of the brightness temperatures within ± 1 K.

[18] Radiosondes are launched twice a day during normal operation at Nauru, and were launched 3–4 times a day during the Nauru99 period. Westwater *et al.* [2000] show that the Vaisala RAOBs launched at the Nauru site during the Nauru99 experiment exhibit the well-known dry bias in precipitable water vapor [Miller *et al.*, 1999]. Therefore we use the radiosondes only for temperature profiles and the shape of the water vapor profile, and to estimate the radar attenuation due to water vapor, which is discussed in section 4.3.

3.2. Prior Probability Density Function

[19] To calculate the microphysical properties of liquid clouds requires knowledge of the droplet size distribution, which cannot be measured directly by remote sensing instruments. However, the radiatively important properties of liquid clouds: liquid water content, shortwave extinction, and effective radius, are all related to the moments of the DSD. Since the remotely sensed parameters of the cloud, radar reflectivity and total liquid water path, are also related to moments of the DSD, we can reduce our requirements to knowing the second, third, and sixth moments of the DSD, plus the relationships between these moments. The prior pdf, $p_{\text{pr}}(\mathbf{x})$, of the state vector, \mathbf{x} , represents our knowledge about the microphysics of a given cloud regime. For our liquid water cloud retrieval, the variables in the prior pdf are the second, third, and sixth moments of the droplet distribution plus the total column precipitable water vapor. The above moments are directly related either to the observed quantities or to the cloud properties we wish to retrieve and the precipitable water vapor is related to the observed microwave brightness temperatures.

[20] To create a functional form of the prior pdf, we assume that the probability of the moments of the droplet size distribution and the total precipitable water vapor, V , are independent, then the prior pdf can be written as

$$p_{\text{pr}}(\mathbf{x}) = p_{\text{pr}}(\mathbf{M}_2, \mathbf{M}_3, \mathbf{M}_6) p_{\text{pr}}(V), \quad (4)$$

where \mathbf{M}_2 , \mathbf{M}_3 , \mathbf{M}_6 are the vertical profiles of the second, third, and sixth moments of the droplet size distribution. For simplification, we can write the prior pdf as $p_{\text{pr}}(\mathbf{M}) p_{\text{pr}}(V)$, where \mathbf{M} is a vector containing the vertical profiles of the second, third, and sixth moments. We model the prior pdf of the precipitable water vapor, $p_{\text{pr}}(V)$, as a Gaussian distribution with mean and standard deviation derived from a climatology of MWR observations at Nauru. We develop a form for the prior pdf of the droplet moments, $p_{\text{pr}}(\mathbf{M}_2, \mathbf{M}_3,$

$\mathbf{M}_6)$, based on data from microphysical probes on in situ aircraft.

[21] The prior pdf should be representative of the cloud regime being retrieved; in this case, shallow boundary layer cumulus such as those primarily seen at Nauru. As there are no in situ microphysical aircraft data available over Nauru, we use data from the Small Cumulus Microphysics Study (SCMS) field project [French *et al.*, 2000], which took place in east central Florida in the summer of 1995 and focused on shallow warm cumuli, and the Joint Hawaiian Warm Rain Project (JHWRP) [Raga *et al.*, 1990], which took place off the northeastern coast of Hilo during the summer of 1985 and sampled shallow cumulus band clouds. In general, the SCMS clouds were small isolated cumuli in their early stages. Cloud depths ranged from 1.5 to 2 km and diameters were roughly 1 km [French *et al.*, 2000]. The JHWRP clouds had bases from 430 to 750 m with tops reaching several hundred meters above the base of the trade inversion (which was generally between 1700 and 2450 m), and occurred in bands that formed approximately 15–20 km off the coast [Raga *et al.*, 1990].

[22] To construct the prior pdf of the droplet size distribution moments, we use measured size distributions sampled every second from the FSSP 100 and Optical Array Probe (OAP) 260X (which measures large droplets) instruments on the National Center for Atmospheric Research (NCAR) C-130 aircraft during SCMS and on the University of Wyoming King Air during JHWRP. During the SCMS project, the FSSP 100 had 15 bins with center diameters from 3.7 μm to 50.5 μm , while the OAP 260X had 64 channels with 17 μm diameter spacing. The first three channels of the 260X probe were noisy (S. Lasher-Trapp, personal communication, 2000) so usable data consists of the 68 μm diameter bin through 1071 μm diameter. During the JHWRP project, the FSSP and 260X were in normal operating modes, with the FSSP measuring droplets from 2.0 μm to 47.0 μm in 3.0 μm bins and the 260X measuring droplets from 40.0 μm to 140 μm in 10.0 μm width bins [Baumgardner, 1989]. Information from the 260X probe is included because a few large droplets can make a substantial contribution to radar reflectivity while contributing negligibly to liquid water content. Figure 2 shows a sample SCMS size distribution that contains both cloud and drizzle droplets. The drizzle droplets are not noticeable in the droplet number concentration, only slightly noticeable in the third moment, but then dominate the sixth moment. Thus the relationship between the sixth and third moments (reflectivity and liquid water content) and sixth and second moments (reflectivity and extinction) will be different for volumes containing only cloud droplets and volumes containing cloud and drizzle droplets, and both need to be included in the prior pdf.

[23] To create the prior pdf, data from 10 SCMS flights and 40 JHWRP flights were used. For each flight we calculate the second, third, and sixth moments of the droplet size distribution for each point in the flight where the FSSP concentration $> 10 \text{ cm}^{-3}$. The moments of the droplet size distribution are given by

$$M_k = \sum_j N_j \left(\frac{D_c}{2} \right)^k, \quad (5)$$

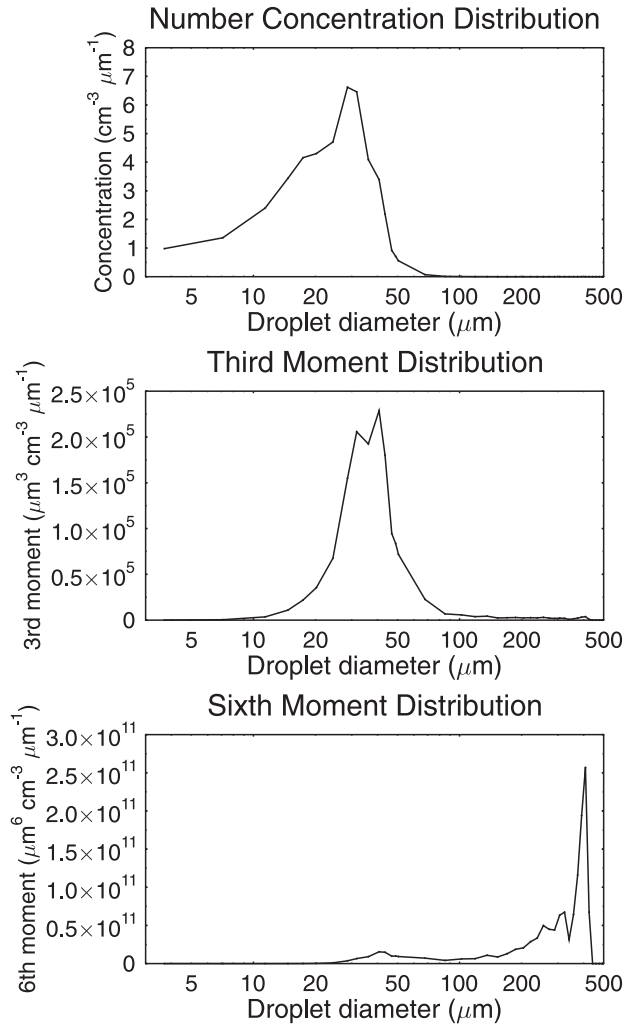


Figure 2. Example SCMS moment distributions for cloud droplet distribution containing some drizzle droplets.

where D_c is the diameter of the center of the FSSP or 260X bin and N_j is the concentration [cm^{-3}] per bin. The units of the k th moment are $\mu\text{m}^k/\text{cm}^3$.

[24] Figure 3 shows scatterplots of the second, third, and sixth moments of the observed droplet distributions from the combined SCMS and JHWRP in situ data. We apply thresholds to the in situ data, based on the detectability limits of the cloud radar and microwave radiometer, of 9.66 on $\log M_6$ (corresponding to -60 dBZ) and 7.0 on $\log M_3$ (corresponding to roughly 1.1 g/m^2 for a 250 m thick cloud). We then fit a 3-D bimodal lognormal probability density function to the data by maximum likelihood estimation. The resulting pdf has 19 parameters: means and standard deviations for each of the moments in each mode of the lognormal distribution, correlations between the moments in each mode and a parameter that represents the relative probability of each mode. The pdf is also shown in Figure 3.

[25] Cloud properties usually have some degree of vertical correlation, however, the prior pdf of M_2 , M_3 , M_6 is obtained from in situ aircraft measurements at various heights above cloud base in different clouds, so no infor-

mation about vertical correlation is present. To estimate a vertical correlation, we examine three months of MMCR data at Nauru. We determine the vertical autocorrelation function of $\log Z_i^{1/2}$ for all liquid water clouds ≥ 20 range gates thick, where Z_i is the reflectivity at each 45 m resolution range gate, i , and $\log Z_i^{1/2}$ is a proxy for $\log M_3$ at the given range gate. We fit an exponential function to the autocorrelation as a function of range gate lag to obtain the decorrelation length. Figure 4 shows the autocorrelation function and the exponential fit. The estimated decorrelation length is 7.2 range gates.

4. Bayesian Retrieval

[26] Applying Bayes' theorem gives the posterior probability distribution for the state vector. To calculate the posterior pdf, we need to develop a forward pdf which relates the state vector, \mathbf{x} , to the measurement vector, \mathbf{y} .

4.1. Forward Probability Density Function

[27] The forward pdf, $p_f(\mathbf{y}|\mathbf{x})$, represents the probability of making the remote sensing observations of brightness temperature and radar reflectivity given a set of cloud properties (profiles of second, third, and sixth moments) and total column water vapor. The forward pdf can be written as

$$p_f(\mathbf{y}|\mathbf{x}) = p_f(T_{b,23}, T_{b,31}, \mathbf{Z} \mid \mathbf{M}_2, \mathbf{M}_3, \mathbf{M}_6, V), \quad (6)$$

where $T_{b,23}$ and $T_{b,31}$ are the microwave brightness temperatures at 23.8 and 31.4 GHz, respectively, and \mathbf{Z} is the vertical profile of radar reflectivity, $\mathbf{Z} = (Z_1, Z_2, \dots, Z_N)$. If we assume that the errors in brightness temperature and reflectivity are independent, that microwave brightness temperatures depend only on the absorption due to cloud liquid water, water vapor, and other gases, and that the reflectivity at each range gate is a function only of the sixth moment, then

$$p_f(\mathbf{y}|\mathbf{x}) = p_{f_T}(T_{b,23} \mid \mathbf{M}_3, V) p_{f_T}(T_{b,31} \mid \mathbf{M}_3, V) \prod_{i=1}^N p_{f_Z}(Z_i \mid M_{6i}), \quad (7)$$

where Z_i and M_{6i} are the reflectivity and sixth moment, respectively, at each range gate and N is the number of cloudy range gates.

[28] To relate the brightness temperatures to the state vector, we use the *Rosenkranz* [1998] microwave absorption model to calculate the volume absorption coefficient at 23.8 and 31.4 GHz at each level of the profile using the temperature, pressure, and shape of the water vapor profile determined from the closest radiosonde, the precipitable water vapor from the prior pdf, and liquid water content calculated from the given M_{3i} . Using the Rayleigh–Jeans approximation, we integrate the radiative transfer equation to calculate the downwelling brightness temperatures at the surface for each frequency. We assume that the forward pdfs of $T_{b,23}$ and $T_{b,31}$ are normally distributed about the simulated brightness temperatures for each observation, with standard deviations equal to the uncertainty in the measured brightness temperatures and model error, σ_{T_b} :

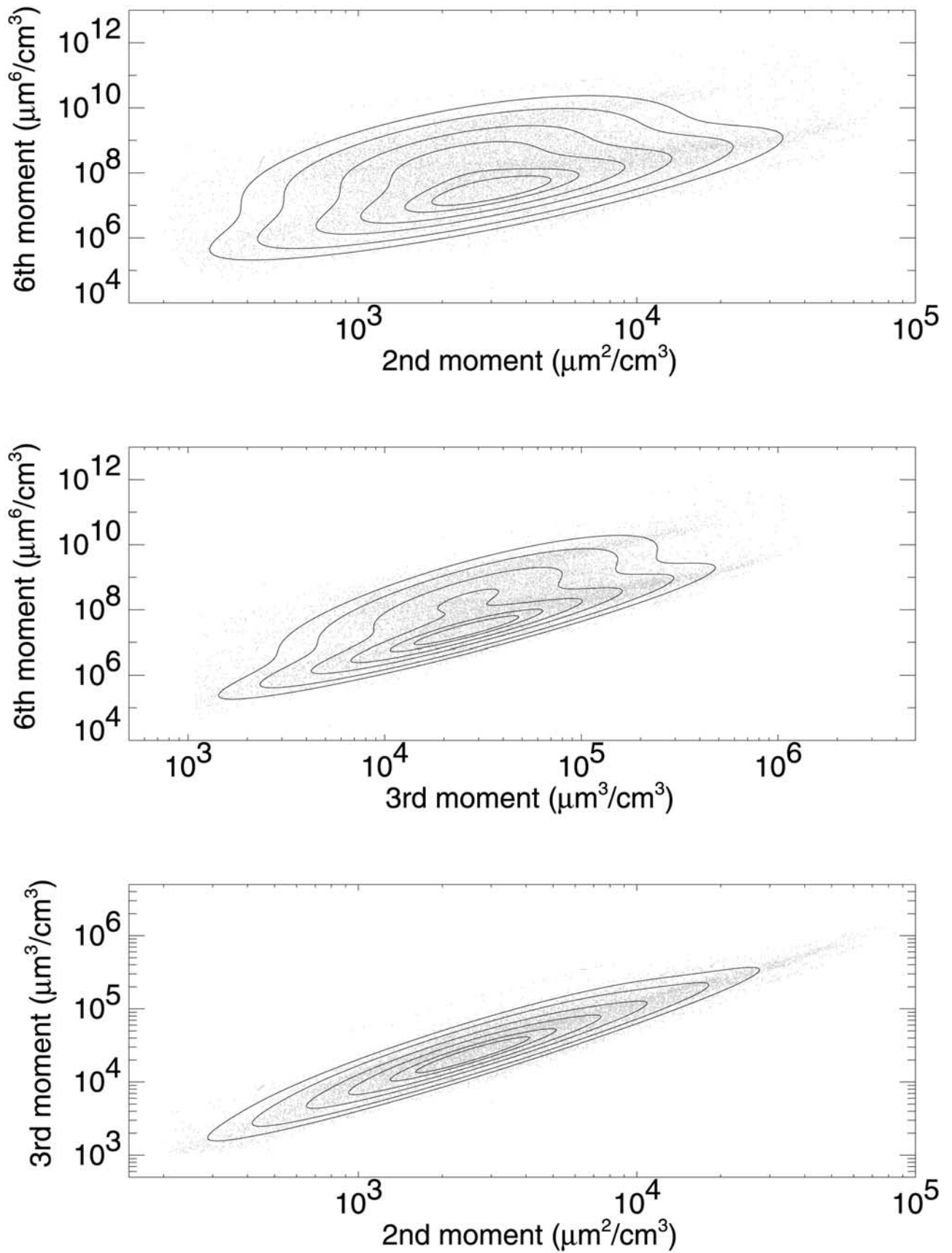


Figure 3. Scatterplots of the cloud droplet moments from the SCMS and JHWRP in situ data. The solid lines are contours of the bimodal lognormal pdfs fit to the data by maximum likelihood.

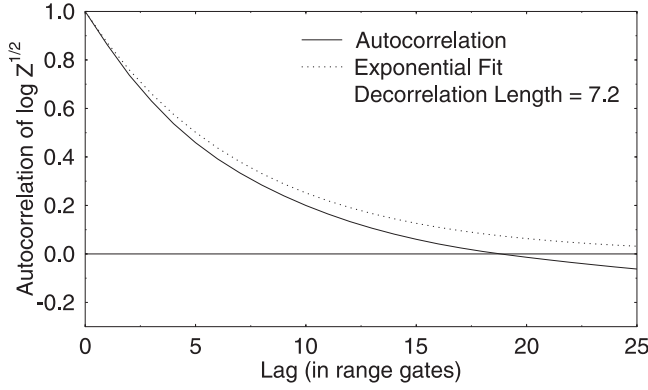


Figure 4. Autocorrelation function of three months of radar data at Nauru. The dashed line is the exponential fit, which gives a decorrelation length of 7.2 range gates.

$$p_{f_r}(T_{b,23} | \mathbf{M}_3, V) = \frac{1}{\sqrt{2\pi} \sigma_{T_{b,23}}} \exp \left[-\frac{(T_{b,23} - T_{bsim,23})^2}{2\sigma_{T_{b,23}}^2} \right] \quad (8)$$

$$p_{f_r}(T_{b,31} | \mathbf{M}_3, V) = \frac{1}{\sqrt{2\pi} \sigma_{T_{b,31}}} \exp \left[-\frac{(T_{b,31} - T_{bsim,31})^2}{2\sigma_{T_{b,31}}^2} \right]. \quad (9)$$

For simplification, we define

$$\chi^2 = \left[\left(\frac{T_{b,23} - T_{bsim,23}}{\sigma_{23}} \right)^2 + \left(\frac{T_{b,31} - T_{bsim,31}}{\sigma_{31}} \right)^2 \right], \quad (10)$$

then the forward pdf of the brightness temperatures becomes

$$p_{f_r} = \frac{\exp(-\frac{1}{2}\chi^2)}{2\pi\sigma_{T_{b,23}}\sigma_{T_{b,31}}}. \quad (11)$$

[29] The forward pdf for the radar reflectivity at a range gate, given the sixth moment, $p_{f_z}(Z_i | M_{6i})$, is represented by a probability distribution around M_{6i} including the two sources of error: calibration error and random error due to the receiver noise. The calibration error on the MMCR at Nauru is assumed to be 1 dB (E. Clothiaux, personal communication, 2000). The receiver noise is the random error associated with the measured signal due to the thermal noise in the radar receiver. It depends on the mode used and the distance of the hydrometeors from the antenna. For each mode, we estimate the sensitivity at each range gate based on the parameters of the operational modes at Nauru given by Clothiaux *et al.* [1999]. If radar reflectivity is expressed in units of mm^6/m^3 , then the calibration error is multiplicative while the receiver noise error is additive.

4.2. Integration Details

[30] To retrieve a vector of the desired cloud properties and a measure of their uncertainty, we integrate over the posterior pdf, to calculate the first and second moments of each parameter, as given in equations (2) and (3). Given the above equations for the prior and forward pdfs, equation (2) can be rewritten as

$$\langle \mathbf{x} \rangle = \frac{\int \mathbf{x} e^{-\chi^2/2} p_{pr}(V) p_{pr}(\mathbf{M}) \prod_i^N p_{f_z}(Z_i | M_{6i}) d\mathbf{x}}{\int e^{-\chi^2/2} p_{pr}(V) p_{pr}(\mathbf{M}) \prod_i^N p_{f_z}(Z_i | M_{6i}) d\mathbf{x}}. \quad (12)$$

This is a $3N + 1$ dimensional integral over the profile of M_2 , M_3 , and M_6 at each range gate and the total column water vapor. The integral could be performed by a Monte Carlo computation, in which random points are uniformly distributed over the integration region. However, the range of observed reflectivities for which a retrieval can be performed is rather large (-60 dBZ to 0 dBZ) while the uncertainty on the observed radar reflectivity is approximately 1 dBZ. Therefore $p_{f_z}(Z_i | M_{6i})$ is vanishingly small in all except a very limited area of the integration region. Since there are many cloudy range gates, performing an accurate Monte Carlo integration over the whole region would require too many points to be computationally feasible.

[31] To reduce the number of points needed in the Monte Carlo integration, we perform a change of variables so that the integration points are randomly distributed according to the prior pdf and the measured Z_i . From the definition of conditional probability,

$$p(M_{6i}, Z_i) = p(Z_i | M_{6i}) p(M_{6i}) = p(M_{6i} | Z_i) p(Z_i). \quad (13)$$

Since $Z_i = aM_{6i}$, where a is simply the constant factor relating reflectivity to the sixth moment, $p(M_{6i})$ is proportional to $p(Z_i)$. Therefore $p_{f_z}(Z_i | M_{6i})$ is proportional to $p_{f_z}(M_{6i} | Z_i)$, and equation (12) can be rewritten as

$$\langle \mathbf{x} \rangle = \frac{\int \mathbf{x} e^{-\chi^2/2} p_{pr}(V) p_{pr}(\mathbf{M}) \prod_i^N p_{f_z}(M_{6i} | Z_i) d\mathbf{x}}{\int e^{-\chi^2/2} p_{pr}(V) p_{pr}(\mathbf{M}) \prod_i^N p_{f_z}(M_{6i} | Z_i) d\mathbf{x}}, \quad (14)$$

where the proportionality constants cancel out. This redefinition of the forward probability allows us to distribute \mathbf{M}_6 around the measured reflectivity according to the noise characteristics of the reflectivity.

[32] We can also rewrite the prior pdf of the droplet distribution moments as

$$\begin{aligned} p_{pr}(\mathbf{M}) &= p_{pr}(M_2, M_3 | M_6) p_{pr}(M_6) \\ &= p_{pr}(M_2, M_3 | M_6) \prod_i^N p_{pr}(M_{6i}), \end{aligned} \quad (15)$$

where $p_{pr}(M_{6i})$ is the marginal prior distribution of M_6 . This allows us to write the retrieval equation as

$$\langle \mathbf{x} \rangle = \frac{\int \mathbf{x} \exp(-\frac{1}{2}\chi^2) \prod_i^N p_{pr}(M_{6i}) d\mathbf{u}}{\int \exp(-\frac{1}{2}\chi^2) \prod_i^N p_{pr}(M_{6i}) d\mathbf{u}}, \quad (16)$$

$$d\mathbf{u} = p_{pr}(V) p_{pr}(M_2, M_3 | M_6) \prod_i^N p_{f_z}(M_{6i} | Z_i) d\mathbf{x}. \quad (17)$$

Through this change of variables we can randomly distribute the integration points according to the prior pdf and the

observed radar reflectivity rather than having to distribute them over the whole state vector space.

[33] To create the random distribution of integration points, we use the model of forward probability, $p_{\mathbf{F}}(M_{6i}|Z_i)$, to create random M_{6i} points given the observed radar reflectivity, Z_i and the sources of error. The calibration error is given by $E_{\text{calib}} = 10^{0.1(r-C)}$ where r is a random Gaussian deviate (which is the same for the entire radar column) and C is the calibration error in dB. The receiver noise at each range gate is $E_{\text{rec},i}$, which is a random deviate with magnitude of the order of the radar sensitivity expressed in mm^6/m^3 . The receiver noise is a significant error until the radar power is at least 10 dB over the noise level. So, at each range gate,

$$M_{6i} = \frac{1}{a} (Z_i E_{\text{calib}} + E_{\text{rec},i}). \quad (18)$$

[34] Given the M_{6i} , we then generate random pairs of (M_{2i}, M_{3i}) from the 3-D bimodal lognormal prior pdf by using analytical expressions which relate the parameters of a 3-D normal pdf to a 2-D conditional normal pdf with a fixed third parameter. The profile of (M_{2i}, M_{3i}) has vertical correlation given by the decorrelation length determined in section 3.2. We then perform the Monte Carlo integration over these points. Further details of the generation of the (M_{2i}, M_{3i}) points are given in Appendix A.

[35] The formulas for the mean and variance of the liquid water content, L , at each range gate, i , can be written as

$$\langle L(i) \rangle = \frac{\sum_{n=1}^{N_{\text{int}}} L_n(i) e^{-\chi_n^2/2} \prod_i^N p_{\text{pr}}(M_{6i,n})}{\sum_{n=1}^{N_{\text{int}}} e^{-\chi_n^2/2} \prod_i^N p_{\text{pr}}(M_{6i,n})} \quad (19)$$

$$\sigma_{L(i)}^2 = \frac{\sum_{n=1}^{N_{\text{int}}} (L_n(i) - \langle L(i) \rangle)^2 e^{-\chi_n^2/2} \prod_i^N p_{\text{pr}}(M_{6i,n})}{\sum_{n=1}^{N_{\text{int}}} e^{-\chi_n^2/2} \prod_i^N p_{\text{pr}}(M_{6i,n})}, \quad (20)$$

where $L(i) = (4\pi/3)(10^{-6}) M_{3i}$ for L in g/m^3 and N_{int} is the number of random points used in the integration. Similar equations can be written for volume extinction and effective radius. The formulas for the mean and variance of the optical depth are

$$\langle \tau \rangle = \frac{\sum_{n=1}^{N_{\text{int}}} \left(\delta R \sum_{i=1}^N \beta_i \right) e^{-\chi_n^2/2} \prod_i^N p_{\text{pr}}(M_{6i,n})}{\sum_{n=1}^{N_{\text{int}}} e^{-\chi_n^2/2} \prod_i^N p_{\text{pr}}(M_{6i,n})} \quad (21)$$

$$\sigma_{\tau}^2 = \frac{\sum_{n=1}^{N_{\text{int}}} \left[\left(\delta R \sum_{i=1}^N \beta_i \right) - \langle \tau \rangle \right]^2 e^{-\chi_n^2/2} \prod_i^N p_{\text{pr}}(M_{6i,n})}{\sum_{n=1}^{N_{\text{int}}} e^{-\chi_n^2/2} \prod_i^N p_{\text{pr}}(M_{6i,n})}, \quad (22)$$

where $\beta_i = 2\pi 10^{-3} M_{2i}$ is the shortwave extinction in km^{-1} and δR is the range gate resolution in kilometers. A similar expression can be written for the retrieved liquid water path.

[36] Since the retrieved parameters are weighted by $e^{-\chi_n^2/2}$, which falls off rapidly with χ^2 , we reduce computational

time by only summing over points for which $\chi^2 < 20$. For a retrieval to be successful, we require at least two points be included in the summation. If the actual cloud properties lie outside the region covered by the prior pdf, then they cannot be retrieved because the values of χ^2 will be too large. Figure 5 shows a flowchart of the steps followed to perform a retrieval.

4.3. Algorithm Details

[37] In the forward pdf for brightness temperature given in equation (8), the parameter σ_{Tb} represents the uncertainty in the brightness temperatures. This uncertainty is a combination of the uncertainty in the measured value and uncertainties in the microwave radiative transfer model. We use a base value of 1.0 K to represent the calibration and model uncertainties. Another source of error is that the MWR and MMCR have very different beam widths (6° and 0.31° , respectively) which means the MWR sees a much larger volume than the MMCR. If the cloud is inhomogeneous or not large enough to fill the entire MWR beam width, then the measured brightness temperatures and radar reflectivities are not representative of the same cloud. To account for this uncertainty, we assume that the T_b error due to the MMCR and MWR beam mismatch is proportional to the LWP of the cloud. We estimate the change in brightness temperature per g/m^2 of liquid water path, ΔT_b , for each frequency from a multiple regression of brightness temperatures to total LWP and precipitable water vapor. Then $\sigma_{T_b}^2 = \sigma_{\text{const}}^2 + \sigma_{\text{frac}}^2$, where $\sigma_{\text{const}} = 1.0$ K, $\sigma_{\text{frac}} = 0.1 \Delta T_b$, and we have assumed the fractional error is 10%.

[38] We correct radar reflectivity for attenuation due to water vapor absorption using the radiosonde humidity profile. Due to the high humidities at Nauru (mean column precipitable water vapor $\sim 4.4 \text{ g}/\text{m}^2$), the two-way attenuation due to water vapor is typically 0.3–0.5 dB at cloud top. Attenuation due to liquid droplets may also be important in thick clouds. At 35 GHz attenuation due to liquid is approximately 0.65 dB km^{-1} per g/m^3 of liquid water at 20°C [Lhermitte, 1990]. We make a first order correction for liquid water attenuation by assuming as a first guess that the statistical LWP calculated from the MWR is correct and that $\text{LWC} \propto Z^{1/2}$ and calculating the attenuation due to that profile [Frisch et al., 1998]. We then adjust the observed radar reflectivities by the calculated attenuation and use the corrected radar reflectivity profile in the retrieval.

[39] We do not attempt to perform retrievals for precipitating clouds; however, precipitation events can lead to raindrops standing on the dome of the MWR after the precipitation has ceased, which causes high brightness temperatures even in clear skies. The MWRs at the ARM sites have been fitted with heaters to speed up the evaporation of rain, but at Nauru, due to the high humidities and perhaps malfunctioning of the heaters, it can take several hours for the rain to evaporate off the dome. This can be seen in Figure 6 which shows a time series of 31 GHz brightness temperature and radar reflectivity. The peak in brightness temperature occurs during precipitation, then the brightness temperature falls off as rain on the dome evaporates. This can mask or artificially inflate the brightness temperature signal due to clouds during this time, although the radar still gives useful information.

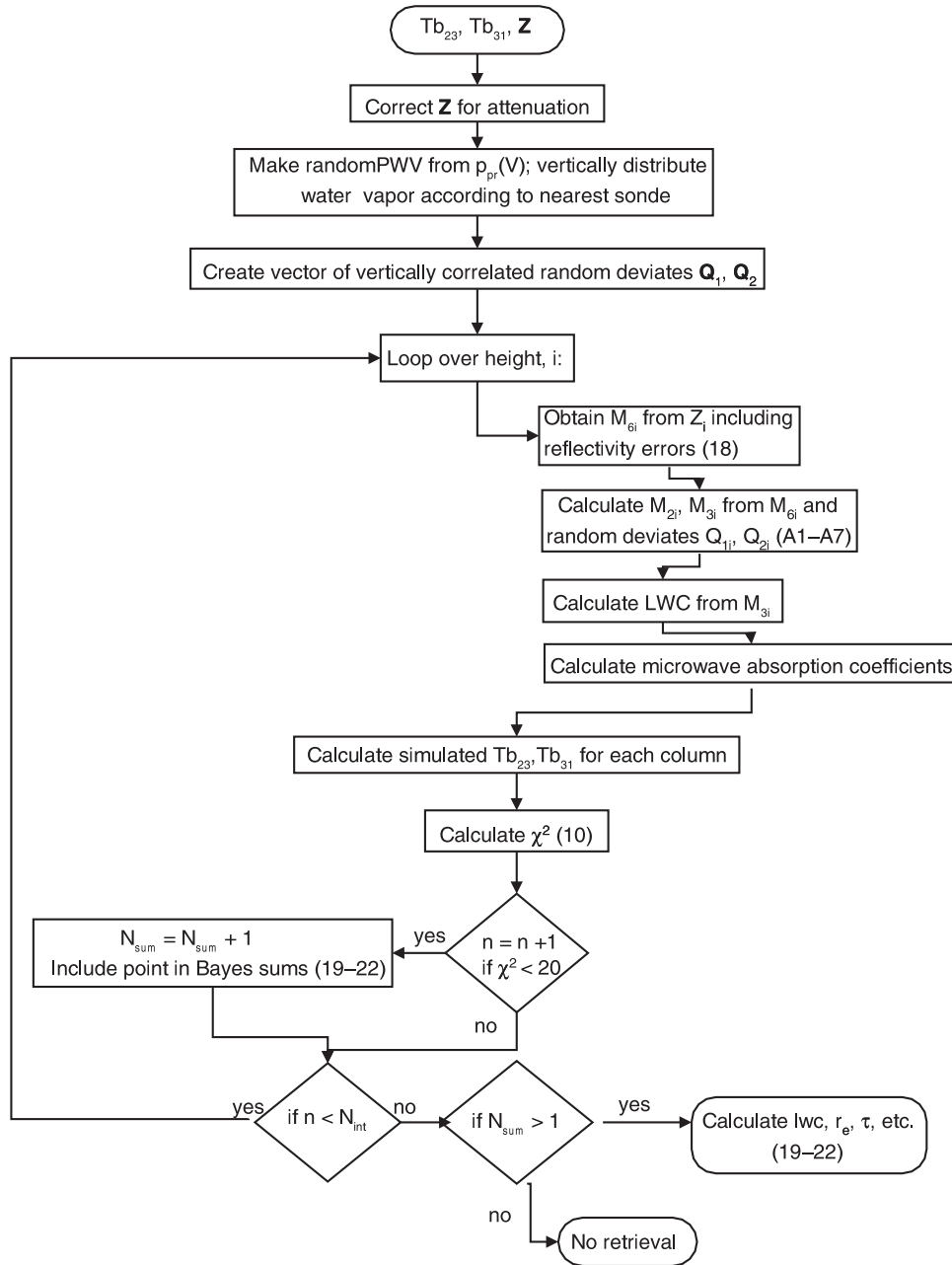


Figure 5. Flowchart of steps taken for each observed reflectivity profile and set of microwave brightness temperatures. Numbers in parentheses refer to equations in the text. N_{int} is the total number of Monte Carlo integration points, n is an indexing variable, and N_{sum} is the number of points having $\chi^2 < 20$.

[40] To correct for the effect of rain on the MWR dome, we identify precipitation events based on a flag in the MWR data stream, brightness temperatures above 100 K, and radar reflectivity in the lowest two range gates. Using the radiosonde profile and the Rosenkranz microwave model, we calculate the slope of the lines relating the 31 and 23 GHz brightness temperatures for clear sky and for liquid cloud conditions. For each cloudy point during which there is water on the radiometer dome after the precipitation has ended, we find the intersection of these two lines given the measured brightness temperatures. This point gives the expected clear sky brightness temperatures. We use the nearest clear points

before and after the cloudy period to estimate what the measured clear sky brightness temperatures would have been during the cloudy period. Then we define the offset due to the water on the dome, ΔT , as the difference between this estimated clear sky brightness temperature and the expected clear sky brightness temperature. To correct for the offset, we subtract ΔT from the measured cloudy brightness temperatures and set $\sigma_{T_b} = \Delta T$.

[41] In the Bayesian algorithm, the retrieval is based on the prior information and the observations. The relative entropy [Bernardo and Smith, 1994; Rodgers, 2000], or information content, defines the amount of information

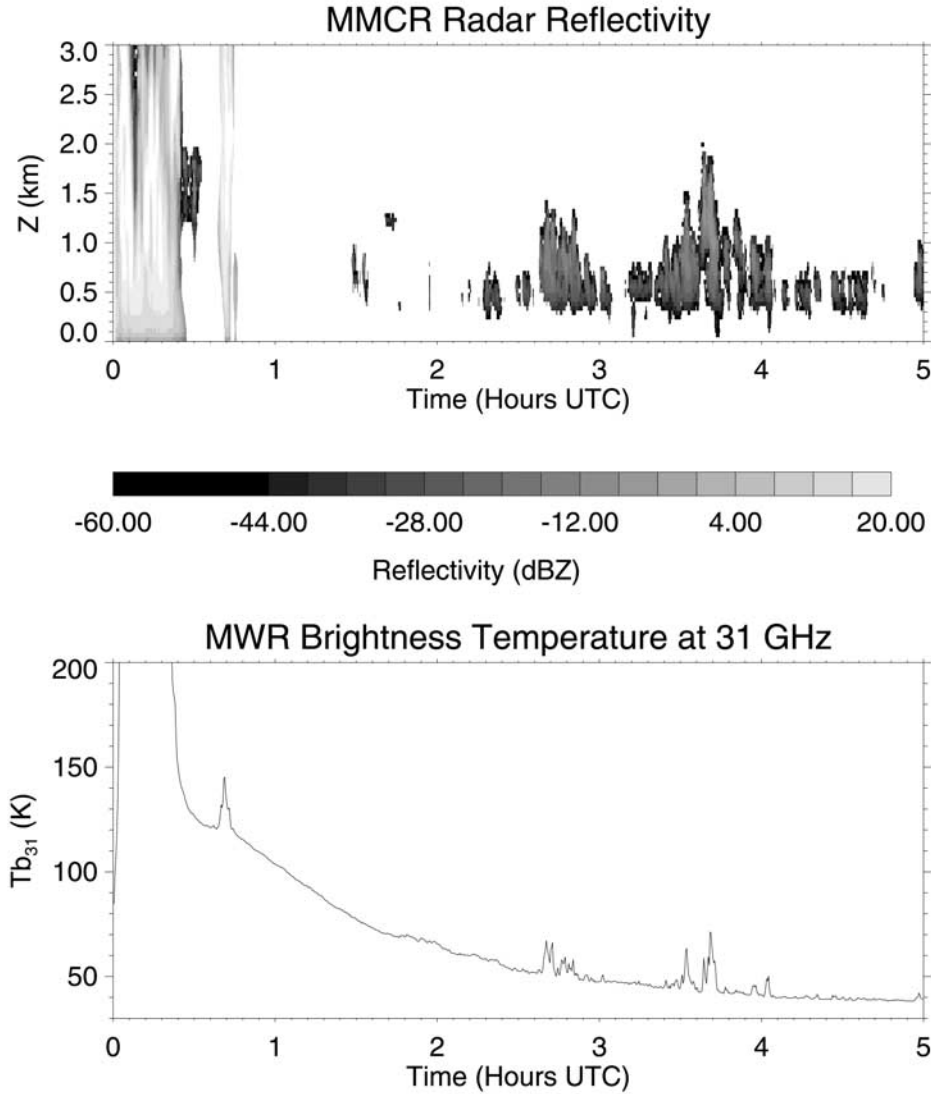


Figure 6. Time series of MMCR reflectivity and MWR 31 GHz brightness temperature at Nauru on 21 July 1999. The brightness temperature peaks at 297 K due to rain, then falls off as the water on the dome evaporates. Note that the signals from the clouds between 01:30 and 02:30 UTC are masked by the signal from the water on the dome.

added to the retrieval by the observation. The relative entropy is defined as

$$I = \int p_{\text{post}}(\mathbf{x}|\mathbf{y}) \ln \left[\frac{p_{\text{post}}(\mathbf{x}|\mathbf{y})}{p_{\text{pr}}(\mathbf{x})} \right] d\mathbf{x}, \quad (23)$$

which is easily computed by integrating over the retrieval points. If the observation adds no information to the retrieval, then the posterior and prior pdfs are the same and the relative entropy is zero. If the observation adds information to the retrieval, then the posterior pdf occupies a small portion of the prior pdf volume and the relative entropy is positive.

[42] The relative entropy can be defined in terms of bits (base 2 units) by dividing by $\ln 2$. One bit of information reduces the uncertainty in the retrieved parameters by a factor of 2, two bits by a factor of 4, etc. For the retrievals

performed over three months of data at Nauru (discussed in section 6), the median relative entropy over all retrieved points was 33.7 bits, due primarily to the fact that the radar reflectivity at each range gate is such a strong constraint on the integration region. Another way to express this is that the volume of parameter space, $(V, \mathbf{M}_2, \mathbf{M}_3, \mathbf{M}_6)$, is reduced from the prior pdf to the posterior pdf typically by a factor of $2^{33.7} = 1.4 \times 10^{10}$.

5. Retrieval Tests

[43] The performance of cloud property retrieval algorithms is often measured by comparing the retrieved cloud properties to the true cloud properties from in situ aircraft measurements [Dong *et al.*, 1997; Sassen *et al.*, 1999]. However, the uncertainties in measurements by aircraft probes (missing small droplets due to instrument thresholds,

under-counting of large droplets due to poor sampling efficiency, coincidence and electronic dead-time losses) as well as disparities in the volumes of air sensed by cloud radars (about 550 m^3 at 1.0 km) and aircraft probes (on the order of $1.0 \times 10^{-3} \text{ m}^3$ for a 30-m height interval during a typical ramp) [Sassen *et al.*, 1999] mean that the DSD measured by the aircraft probes is not necessarily representative of the volume averaged sixth moment measured by the radar at the same time. Since the prior pdf needs merely to be representative of the microphysical relationships in cumulus clouds and not exactly the same droplet size distributions measured by the remote sensors, the uncertainties and sampling issues are less important in the development of the prior pdf than in retrieval comparisons.

[44] Another way to assess the performance of a cloud property retrieval algorithm is to compute simulated MMCR and MWR input observations from cloud fields generated by a cloud model. Since the “true” cloud properties (the cloud model values) are known and the sampling volume is much closer to that of the radar, the uncertainties in the retrieval algorithm can be clearly defined, avoiding the measurement and sampling uncertainties associated with validating remote sensing retrievals against aircraft in situ data. In these types of tests, the cloud model results do not need to be completely accurate simulations of a particular cloud field as long as the simulated cloud properties are representative of the general cloud regime being retrieved. Although we hope to be able to use in situ aircraft measurements to examine the results of our retrieval algorithm in the future, such data do not currently exist over the ARM site at Nauru. Therefore we use maritime trade cumulus cloud fields generated by an explicit binned microphysics large-eddy simulation (LES) model and a radiative transfer scheme to simulate observations to test the retrieval algorithm.

5.1. Details of LES Tests

[45] To test the Bayesian retrieval algorithm, we use results from two different large-eddy simulations of trade cumulus, in which the total condensation nuclei (CN) concentration is fixed at 250 cm^{-3} (case 1) and 150 cm^{-3} (case 2). The details of the LES model are given in Appendix B for interested readers. To simulate maritime trade-wind cumulus similar to that seen at Nauru, we adapt an idealization from Stevens *et al.* [2001] of measurements averaged over the first 5 days of the Atlantic Trade-Wind Experiment (ATEX), characterized as “nearly classic” trade cumulus [Augstein *et al.*, 1973]. The model is run for 8 hours with full output every half hour (model time). The behavior of the model simulation is characterized in Figure 7, where it is seen that the cloud fractional coverage is reduced and precipitation enhanced by the decreased droplet concentrations in case 2. We define “cloud” in the LES results as any grid point with number concentration greater than 10 cm^{-3} , liquid water content greater than 0.005 g/m^3 , and calculated reflectivity greater than -60 dBZ . Figure 8 shows histograms of the radar reflectivity calculated at each cloudy LES grid point for the two cases. Case 2 has more drizzle droplets, as seen by the larger number of points with reflectivities greater than -10 dBZ .

[46] To create the input data needed for the Bayesian retrieval algorithm, we calculate the profile of radar reflectivity (dBZ) from the sixth moment of the LES droplet size distribution, and add random Gaussian noise to simulate a measurement uncertainty of 1 dBZ. We calculate the brightness temperatures at 23.8 GHz and 31.4 GHz at each horizontal grid point from the vertical profile of temperature, water vapor, and liquid water content. We add random Gaussian noise with magnitude 0.5 K to the brightness temperatures to simulate measurement uncertainty. We average the temperature and water vapor at each level over the horizontal grid to create an average “sounding.” The profile of reflectivities and brightness temperatures at each horizontal grid point, and the average sounding are input to the retrieval algorithm for each cloudy scene.

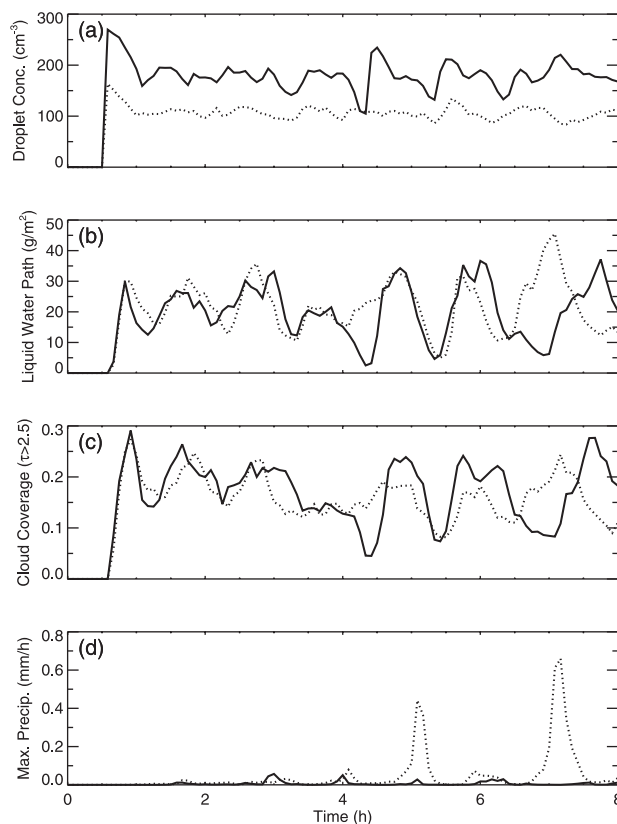


Figure 7. Evolution of (a) droplet concentration (averaged over grid cells with cloud water $> 0.05 \text{ g/kg}$), (b) liquid water path (the horizontally averaged column of cloud water), (c) cloud fractional coverage (the fraction of columns with cloud optical depth for geometric scatterers > 2.5), and (d) maximum precipitation flux at the surface for simulations with total particle concentrations of 250 and 150 cm^{-3} (solid and dotted lines, respectively). Results are plotted as instantaneous values every 5 min.

tivity (dBZ) from the sixth moment of the LES droplet size distribution, and add random Gaussian noise to simulate a measurement uncertainty of 1 dBZ. We calculate the brightness temperatures at 23.8 GHz and 31.4 GHz at each horizontal grid point from the vertical profile of temperature, water vapor, and liquid water content. We add random Gaussian noise with magnitude 0.5 K to the brightness temperatures to simulate measurement uncertainty. We average the temperature and water vapor at each level over the horizontal grid to create an average “sounding.” The profile of reflectivities and brightness temperatures at each horizontal grid point, and the average sounding are input to the retrieval algorithm for each cloudy scene.

5.2. LES Test Results

[47] To assess the performance of the Bayesian retrieval algorithm, we compare the retrieved properties to results obtained from two other retrieval methods. The method of Frisch *et al.* [1995] assumes the droplet distribution is described by a lognormal distribution with the width of the distribution fixed and number concentration, N , constant with height. Profiles of liquid water content are determined from the radar reflectivity by

$$L(i) = C_\sigma \rho_w Z_i^{1/2} N^{1/2}, \quad (24)$$

where ρ_w is the density of water, C_σ is a constant which depends on the chosen width of the distribution, and N is constrained by the integrated liquid water path. For the Frisch algorithm, we calculate a total liquid water path from a statistical regression on the two microwave brightness temperatures.

[48] *Liao and Sassen* [1994] present a radar-only retrieval method based on a reflectivity(Z)-LWC regression equation developed from an adiabatic cloud model for nonprecipitating cumulus and stratocumulus clouds. This equation is given by

$$Z_i = \frac{3.6}{N} L(i)^{1.8}, \quad (25)$$

where $L(i)$ is the liquid water content in g/m^3 , N is mean number concentration (cm^{-3}) and Z_i (mm^6m^{-3}) is the reflectivity calculated from the model size distributions at each grid point. By comparison with empirical relationships, they suggest that a value of $N = 100 \text{ cm}^{-3}$ may be appropriate for a variety of liquid phase clouds.

[49] To investigate the sensitivity of the retrievals to the prior data, we perform two sets of retrievals on the simulated LES observations. The first set represents the performance of the algorithms assuming that the prior data is well known, by creating the prior information from the LES output. The second set of retrievals represents a more realistic scenario, in which the general cloud type being retrieved is known, but not the detailed characteristics of the clouds. For this retrieval, the prior information comes from in situ data from the SCMS and JHWRP field experiments.

[50] In the first set of retrievals, we create prior pdfs for the Bayesian algorithm based on the LES size distribution moments for each of the two cases. The prior pdf and scatterplots of the moments are shown in Figure 9 for case 1. For the radar-regression method, the number concentration is set equal to the average LES number concentration for each case. For the Frisch method, the regression coefficients for the LWP/brightness temperature regression are also determined directly from the LES output. Since the LES model does not assume a fixed form of the size distribution, there is no explicit value for the width of the lognormal size distribution. Therefore we define a lognormal equivalent width,

$$\sigma = \left(\frac{1}{6} \log \left[\frac{\pi}{48} \left(\frac{Z_i \rho_w}{L_i r_{e,i}^3} \right) \right] \right)^{1/2} \quad (26)$$

where ρ_w is the density of water and Z_i is the radar reflectivity, L_i the liquid water content, and $r_{e,i}$ the effective radius at the given grid point, i . We set the width of the lognormal distribution to the mean of the lognormal equivalent width for each case. For the Liao-Sassen regression algorithm, we set N equal to the mean number concentration of each case (165 cm^{-3} for case 1 and 102 cm^{-3} for case 2).

[51] In the second set of retrievals, the prior pdf for the Bayesian data is described in section 3.2. The coefficients for the LWP/brightness temperature regression for the Frisch method are those used operationally for the ARM

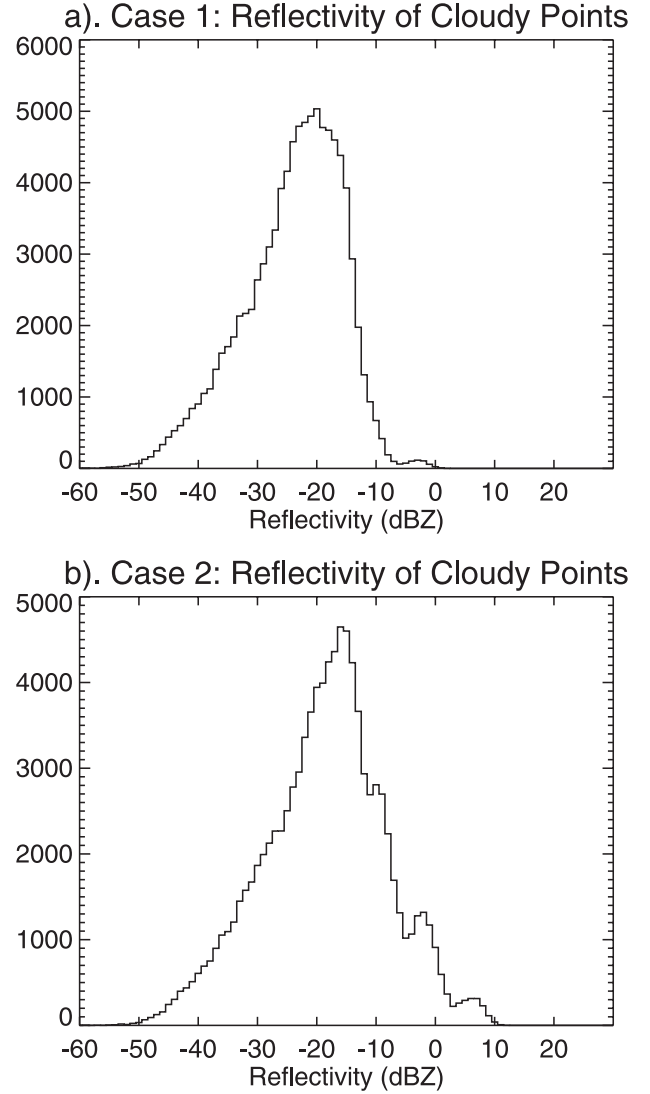


Figure 8. Histograms of radar reflectivity calculated from the LES size distributions at each grid point for (a) case 1 and (b) case 2.

statistical LWP retrievals at Nauru. We use two different values of the lognormal width: $\sigma = 0.35$, which is the value given by *Frisch et al.* [1995] (for stratus clouds); and $\sigma = 0.41$, which is the mean value of the lognormal equivalent width derived from the SCMS/JHWRP in situ data. For the LWC- Z regression algorithm, we use a number concentration of 100 cm^{-3} , as given by *Liao and Sassen* [1994].

[52] We compare the retrieved parameters to the known values from the LES model to assess the errors of each retrieval method. Our primary error statistic is the median fractional error, which is defined such that for all the retrievals being combined for an error estimate, 50% have error less than the median error, and 50% have larger error. The median fractional retrieval errors for each of the methods for the two LES cases are shown in Table 1. For the LWC- Z regression method only liquid water content and liquid water path can be retrieved. Since fractional errors for values near zero are meaningless, we apply the fractional

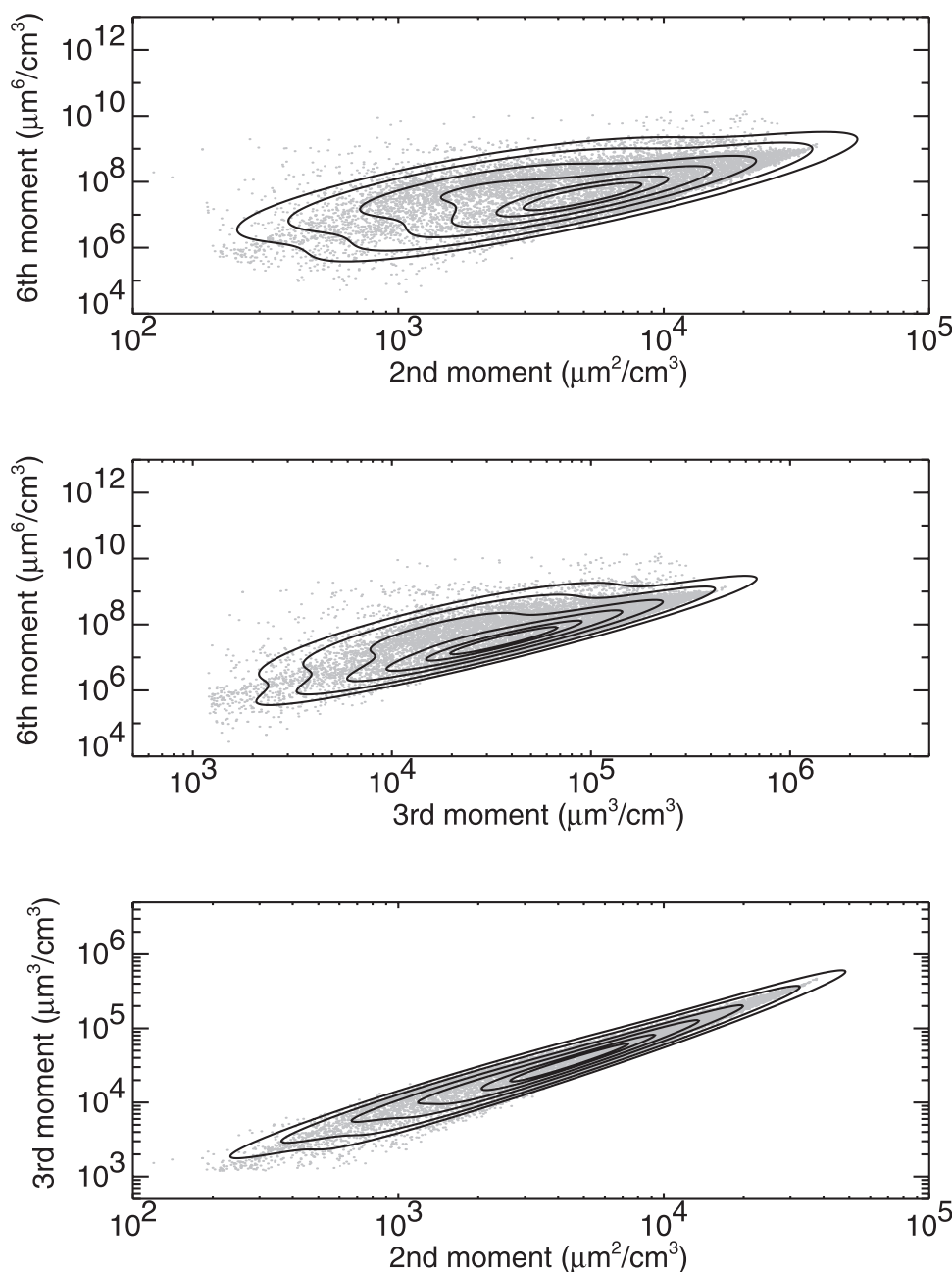


Figure 9. Scatterplots of the cloud droplet moments from the LES cloud fields for case 1. The solid lines are contours of the bimodal lognormal pdfs fit to the data by maximum likelihood.

error to columns with LWP greater than 5 g/m^2 for statistics on LWP and optical depth, τ , and to grid points with LWC greater than 0.02 g/m^3 for statistics on LWC and r_e .

[53] As expected, the radar-only regression method has significantly larger retrieval errors than the combined radar-radiometer methods since it does not have the additional constraint of the microwave radiometer on the droplet size distribution. Additionally, the slope of the distribution was derived from a particular cloud model, which may not be representative of the LES model used in these tests.

[54] The Bayesian and Frisch methods produce roughly the same median fractional errors for LWC. For LWP the Frisch method has smaller errors when using the LES prior information, but larger errors when the more general prior

information is included. The Bayesian algorithm has significantly smaller errors for effective radius and optical depth. The similar magnitude errors for the LWC and LWP illustrate that, given the radar reflectivity and a constraint on the total LWP, retrieved LWC is relatively insensitive to the assumptions about the size distribution [Frisch *et al.*, 1998]. However, the effective radius (and therefore the optical depth) is sensitive to assumptions about the shape of the size distribution. The retrieved r_e from the Frisch method is more sensitive to drizzle, as seen by the larger errors in r_e for case 2.

[55] The large errors in effective radius from the Frisch algorithm are due primarily to the assumption of constant width in the lognormal distribution. Figure 10 shows histo-

Table 1. Median Fractional Errors for All Retrieval Algorithms Over All LES Scenes^a

Method	r_e	LWC	LWP	τ
<i>Case 1: CN = 250; LES Prior Methods</i>				
Bayes	0.096	0.29	0.18	0.22
Frisch $\sigma = 0.35$	0.13	0.28	0.13	0.22
Frisch $\sigma = 0.39$	0.14	0.28	0.13	0.24
LWC-Z	—	1.3	1.76	—
<i>Case 1: CN = 250; General Prior Methods</i>				
Bayes	0.14	0.31	0.18	0.20
Frisch $\sigma = 0.35$	0.19	0.32	0.24	0.29
Frisch $\sigma = 0.41$	0.18	0.32	0.24	0.25
LWC-Z	—	0.73	1.09	—
<i>Case 2: CN = 150; LES Prior Methods</i>				
Bayes	0.098	0.33	0.17	0.22
Frisch $\sigma = 0.35$	0.22	0.30	0.11	0.25
Frisch $\sigma = 0.41$	0.20	0.30	0.11	0.27
LWC-Z	—	2.07	3.36	—
<i>Case 2: CN = 150; General Prior Methods</i>				
Bayes	0.13	0.33	0.17	0.22
Frisch $\sigma = 0.35$	0.35	0.33	0.24	0.33
Frisch $\sigma = 0.41$	0.28	0.33	0.24	0.28
LWC-Z	—	2.02	3.30	—

^aFractional errors for LWC and effective radius, r_e , are defined where $LWC > 0.02 \text{ g/m}^3$; for LWP and optical depth, τ , errors are defined where $LWP > 5$; g/m^2 .

grams of the lognormal equivalent width parameters for the Bayesian retrieval and the LES output as well as the value of 0.41 for the Frisch retrieval for case 2. The LES lognormal equivalent width has a mean of 0.41 and a standard deviation of 0.11 while the retrieved Bayesian equivalent width has a mean of 0.34 and standard deviation of 0.13. While the Bayesian algorithm does not replicate the true equivalent width exactly, it does reproduce much of the variability in the parameter, which leads to more accurate effective radius retrievals. For the Frisch algorithm, using the mean lognormal width from the prior, 0.41, which happens to coincide with the mean value from the LES model, does improve the retrievals compared to using the value of 0.35. For the Frisch method, assuming a value of 0.41 when the width is actually 0.5 leads to an overestimate of effective radius by a factor of 1.3 for a given radar reflectivity and liquid water content. Since the lognormal width is fixed in the Frisch method, the a priori choice of the value is important.

[56] These results also show the extent to which a priori information is important in all of the retrieval algorithms. The errors in the Frisch method increase for all variables when the parameters of the algorithm are specified by the more general prior information rather than taken from the LES data. In contrast, the errors in the Bayesian method stay roughly the same for all variables except effective radius.

[57] Table 2 shows the root mean square (RMS) errors for the Bayesian and Frisch algorithms as well as the mean LES value for each parameter for comparison. Root mean square errors are calculated over all retrieved points. The Bayesian and Frisch algorithms have similar RMS errors for LWC. The Frisch algorithm has smaller RMS error for LWP than the Bayesian algorithm when the LES statistical coefficients are used, but larger error when the ARM coefficients are used. The Bayesian algorithm has lower RMS errors than

the Frisch algorithm for effective radius and optical depth in all cases.

[58] One of the advantages of the Bayesian method is that error bars, defined by one standard deviation, are retrieved for each parameter. Figure 11 shows the retrieved optical depths and error bars from the LES test for the two cases using the Bayesian retrieval algorithm with the prior pdf determined from the SCMS/JHWRP data.

[59] The LES tests can be used to assess the accuracy of the retrieved error bars. Following *Evans et al.* [2002], we define a normalized error, $\delta_q = (q_{\text{ret}} - q_{\text{true}})/\sigma_q$, where q_{ret} and q_{true} are the retrieved and true values of a parameter q , and σ_q is the retrieved standard deviation. Table 3 lists the fraction of cases for which the normalized error is within ± 1 and ± 3 for each of the retrieved variables in the two cases. The normalized errors for all parameters are within ± 1 approximately 54–69% of the time, and within ± 3 for 96–99.7% of the cases, indicating that the error bars are a reasonable measure of retrieval uncertainty for this test.

6. Retrieval Examples From Nauru

[60] In the previous section we examined the results of the Bayesian algorithm using cloud fields simulated by an LES model. In this section we show results from actual retrievals using data at the Nauru ARM site. We used three months of Nauru data, from 1 June 1999 to 31 August 1999. This time period includes the Nauru99 field project which occurred from 15 June 1999 to 15 July 1999. The ARSCL product was used to determine cloud boundaries and locations at 10 s resolution. Cloud phase was based on a simple temperature thresholding method, with temperatures above -10°C assumed to be liquid clouds. Retrievals were attempted for all nonprecipitating liquid water clouds with column maximum reflectivities $< 0 \text{ dBZ}$ (a total of 229,000 columns). We were able to successfully perform retrievals for 225,000 columns, or 98.3% of those attempted. Columns for which retrievals were unsuccessful were often adjacent to columns for which retrievals were not attempted due to precipitation or high reflectivities. Vertical profiles of liquid water content, visible extinction, and effective radius were retrieved as well as column liquid water path and optical depth. Figure 12

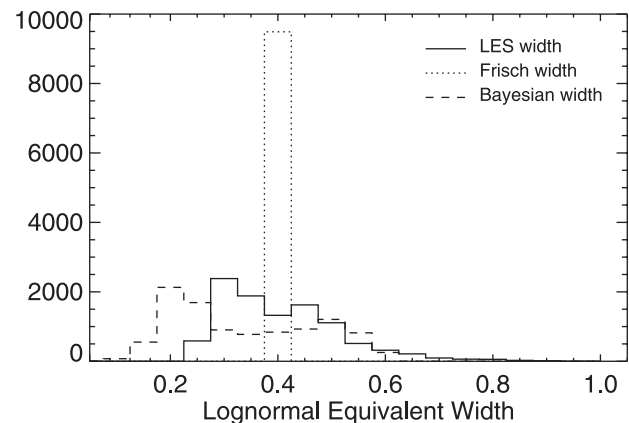


Figure 10. Histograms of the lognormal equivalent width parameter for the Bayesian and Frisch retrievals as well as the true value from the LES model for case 1.

Table 2. Mean Value From LES Model and Root-Mean-Square Errors for Frisch and Bayesian Algorithms Over All LES Scenes for Each Case^a

	Case 1				Case 2			
	r_{es} , μm	LWC, g/m^3	LWP, g/m^2	τ	r_{es} , μm	LWC, g/m^3	LWP, g/m^2	τ
Mean LES value	8.97	0.29	61.3	9.7	11.0	0.33	77.7	10.0
RMS errors								
Bayes LES prior	1.6	0.13	18.9	4.0	1.8	0.20	24.7	4.0
Frisch LES coeffs	4.2	0.12	9.1	3.9	7.8	0.18	9.6	5.7
Bayes in situ	2.0	0.14	18.5	3.2	3.3	0.19	24.7	4.0
Frisch ARM coeffs	5.6	0.15	23.7	4.4	10.1	0.19	25.4	7.1

^aRMS errors include all retrieved points.

shows examples of retrieved liquid water content and effective radius for shallow cumulus at Nauru as well as a time series of retrieved liquid water path and optical depth plus error bars on the retrieved optical depth.

[61] Figure 13 shows histograms of the retrieved effective radius, liquid water content, and liquid water path, and Table 4 shows the mean, median, and standard deviation of the liquid water path, optical depth, liquid water content,

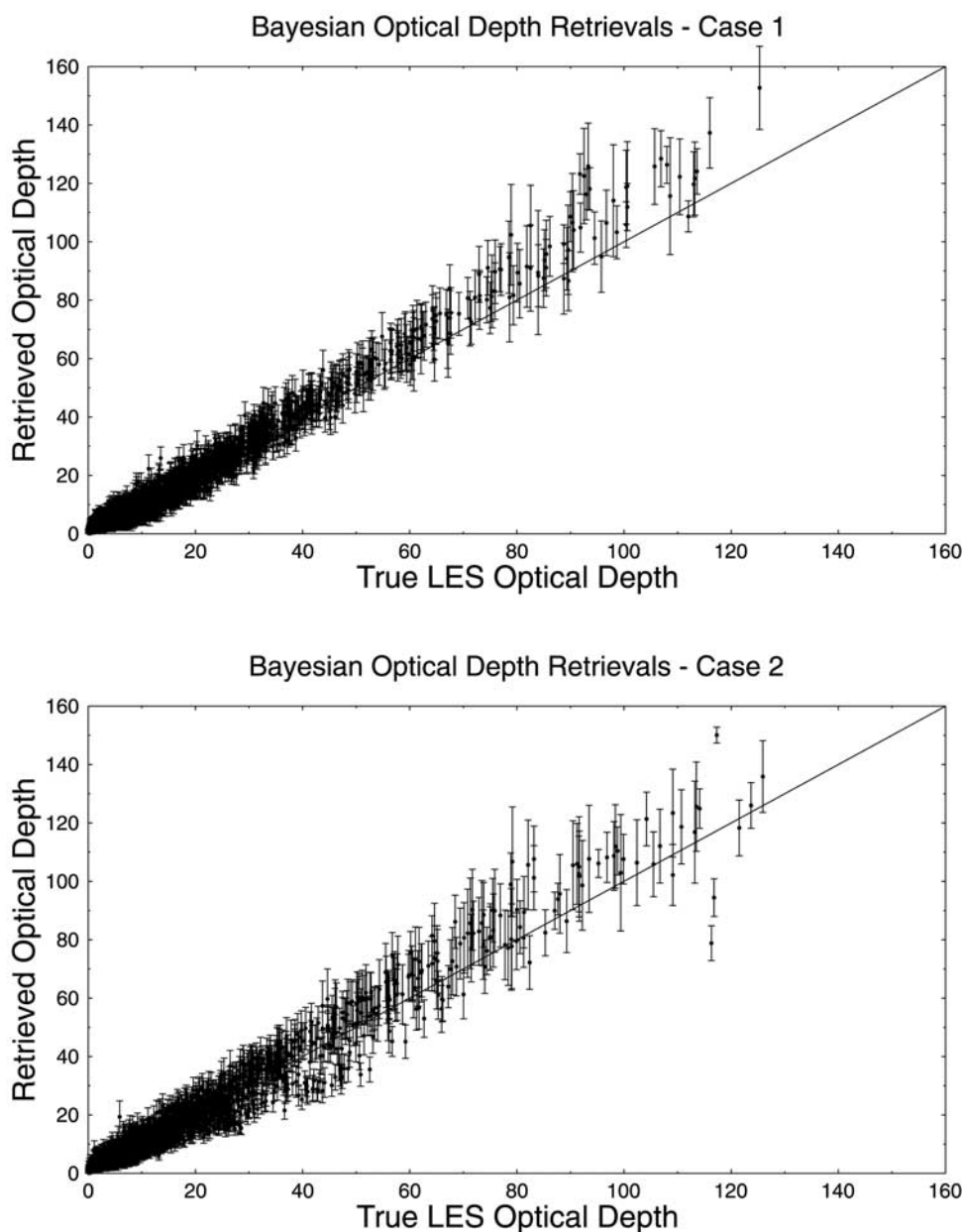
**Figure 11.** Scatterplots of the optical depths (and error bars) retrieved from the LES cloudy scenes using the Bayesian algorithm and the prior pdf based on the SCMS/JHWRP in situ data.

Table 3. Statistics on the Absolute Retrieval Error Normalized by the Bayes Retrieved Error Bars^a

	Case 1		Case 2	
	Fraction δ Within 1σ	Fraction δ Within 3σ	Fraction δ Within 1σ	Fraction δ Within 3σ
LWC	0.63	0.997	0.65	0.994
r_e	0.54	0.977	0.56	0.961
LWP	0.50	0.979	0.59	0.960
τ	0.69	0.996	0.66	0.983

^aThe fraction of cases with normalized errors between ± 1 and ± 3 is listed for each parameter. Results are shown for case 1 and case 2 for the Bayesian retrieval using the SCMS/JHWRP prior.

and effective radius for the retrieved nonprecipitating liquid clouds at Nauru during this time period. These statistics show a rather large range in liquid water path, with a median of only 20.3 g/m², but a standard deviation of 122.4 g/m². The mean retrieved effective radius is 7.8 μ m, which is more typical of marine than continental clouds (e.g., Miles *et al.* [2000] compiled a large number of in situ observations and found an average effective radius of 7.1 μ m for marine stratus/stratocumulus clouds and 4.1 μ m for continental clouds) and may indicate relatively low aerosol concentrations over Nauru. The mean retrieved liquid water content at Nauru is 0.112 g/m³, which is approximately 6% less than that found for marine stratiform clouds by Miles *et al.* [2000]. The retrieved liquid water contents and effective radius might be biased low as retrievals were not performed for clouds that were precipitating or had high radar reflectivity.

[62] Optical depth distributions are often modeled by gamma distributions for radiative transfer applications [Barker, 1996; Oreopoulos and Barker, 1999]. Figure 14 shows a histogram of the retrieved optical depth and the appropriate gamma distribution for this data. The normalized gamma distribution is given by

$$p(\tau) = \frac{1}{\Gamma(\nu)} \left(\frac{\nu}{\mu}\right)^\nu \tau^{\nu-1} \exp(-\nu\tau/\mu), \quad (27)$$

where $\Gamma(\nu)$ is the gamma function and $\nu = (\mu/\sigma)^2$ is a measure of the width of the distribution, and μ and σ are the mean and standard deviation of the optical depth. For the retrieved optical depth at Nauru, μ and σ are given in Table 4 and $\nu = 0.37$. These parameters are consistent with those found by Barker *et al.* [1996] for Landsat scenes that were classified as scattered cumulus. For these scenes, the mean optical depth ranged from 1.036 to 12.059, standard deviation ranged from 0.750 to 26.565, and gamma distribution width ranged from 0.189 to 1.235. A few Landsat scenes classified as broken stratocumulus also had similar parameters, but the majority of the broken stratocumulus had gamma distribution widths greater than 1.0.

7. Summary and Conclusions

[63] This paper describes a new algorithm for retrieving optical depth and vertical profiles of liquid water content and effective radius of liquid water clouds from millimeter wavelength radar reflectivity and dual-channel microwave brightness temperatures. Error bars which represent one

standard deviation are also retrieved for each parameter. This retrieval algorithm is based on Bayes' theorem of conditional probability and combines prior information on cloud microphysics with remote sensing observations. The algorithm was designed to take advantage of the suite of remote sensing instruments available at the ARM sites, which will allow long time series of cloud property retrievals.

[64] Prior probability distribution functions for liquid water clouds at Nauru were developed from in situ aircraft observations of the second, third, and sixth moments of droplet size distributions measured with the FSSP and 260X probes in shallow cumuli over Florida and off the coast of Hawaii. No assumptions about the form of the droplet size distribution were made. A forward pdf for observed brightness temperatures from the MWR, based on the Rosenkranz microwave absorption model, was developed to avoid the problems with the statistical regression retrievals for liquid water path. A forward pdf for the radar reflectivity that includes both calibration error and random noise error was developed.

[65] The retrieved parameter vector is the mean of the posterior probability density function. A computational form of the Bayesian retrieval was described, in which a change of variables is used to distribute integration points randomly according to the prior pdf and the observed radar reflectivity. This drastically reduces the number of integration points needed for the Monte Carlo calculation.

[66] Retrieval experiments were performed using simulated radar reflectivity and microwave brightness temperatures derived from trade cumulus cloud fields from an LES model with explicit microphysics. For liquid water clouds with LWC greater than 0.02 g/m³ and LWP greater than 5 g/m², the overall median fractional errors for the Bayesian algorithm using the prior pdf developed from in situ data are about 0.14 for effective radius, 0.2 for LWP and optical depth, and 0.3 for liquid water content. These errors were significantly less than those from existing radar/radiometer retrieval methods for effective radius and optical depth and similar in magnitude for LWC and LWP. For the Bayesian algorithm, the RMS errors were comparable to those from the Frisch algorithm for LWC and LWP, but were smaller for r_e and τ when the realistic prior information was used. The Bayesian method was shown to be less sensitive to the source of prior information than the Frisch retrieval. The retrieval simulations also demonstrated that the Bayesian algorithm provides reasonable error estimates on the retrieved parameters.

[67] Retrievals were performed on three months of data from Nauru. Over 98% of the columns for which retrievals were attempted produced successful retrievals. Histograms of retrieved liquid water content, effective radius, liquid water path, and optical depth were shown.

[68] This paper illustrates the application of the Bayesian algorithm to trade wind cumulus at Nauru. The algorithm can be easily applied to other liquid cloud regimes if suitable microphysical prior pdfs are developed. This paper also illustrates the use of retrieval simulations to assess the performance of a cloud property retrieval algorithm. Although such algorithms are usually "validated" against in situ measurements of cloud properties, we believe using simulated observations from cloud models is a better way to

Bayesian Retrievals - Nauru 6/05/99

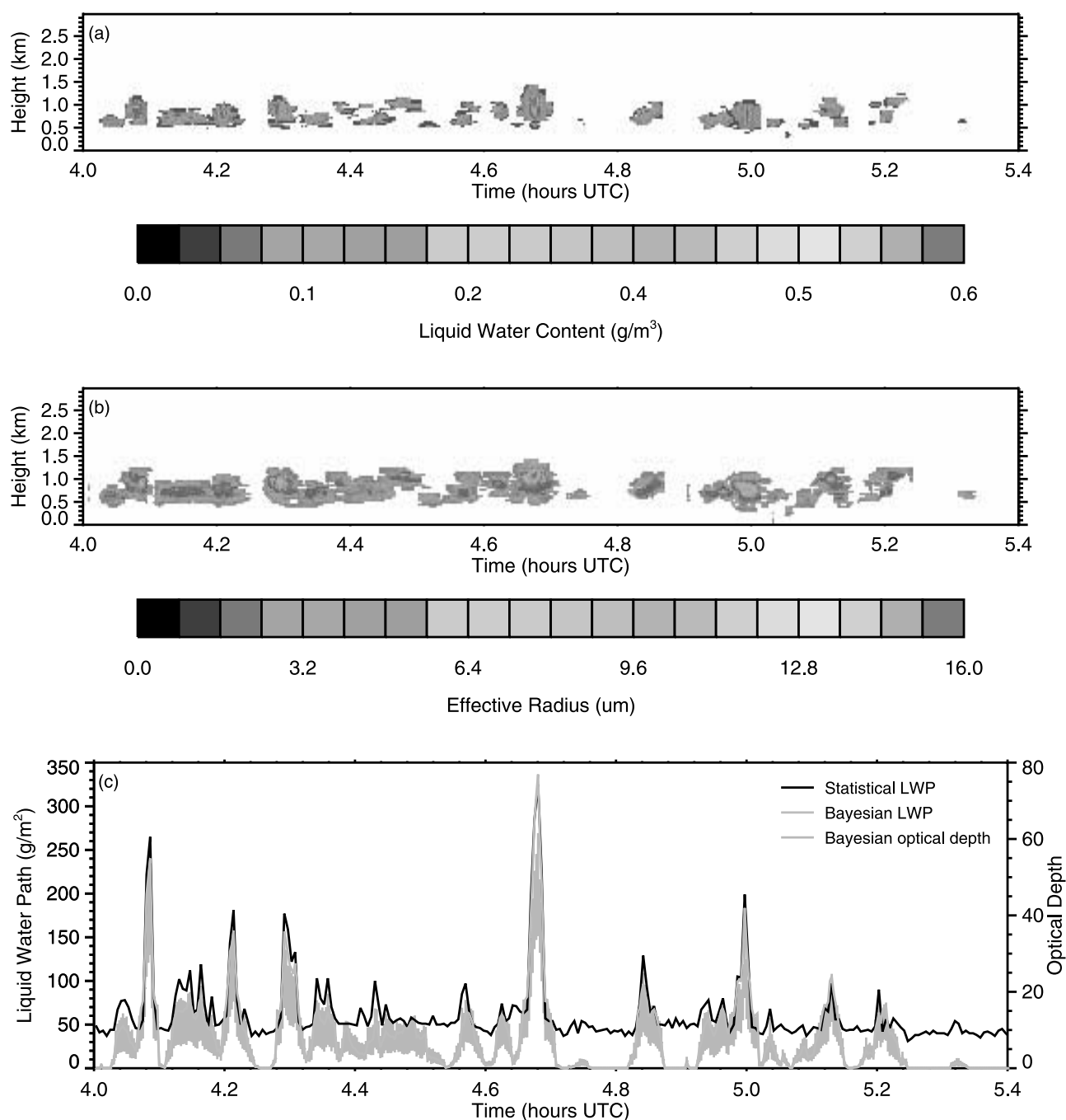


Figure 12. Examples of Bayesian retrievals at Nauru on 5 June 1999. Time–height cross sections of (a) retrieved liquid water content and (b) effective radius. (c) Time series of retrieved liquid water path and optical depth at Nauru. The black line is the ARM retrieved statistical liquid water path during this time. The blue line is the Bayesian retrieved liquid water path, and the green line is the Bayesian optical depth plus error bars. See color version of this figure at back of this issue.

assess the strengths and weaknesses of various algorithms. Since the “true” cloud properties from the cloud model are known, errors in the retrieved parameters can be accurately determined and their causes more easily identified.

[69] The primary purpose of this research is to create a long-term data set of cloud properties that can be used by

other researchers, for example, for developing cloud parameterizations, comparing to model output, or performing radiative transfer calculations. For such purposes, it is important that the retrieved properties and derived products of the algorithm include meaningful error bars so that users of the retrievals (who are not intimately familiar with the

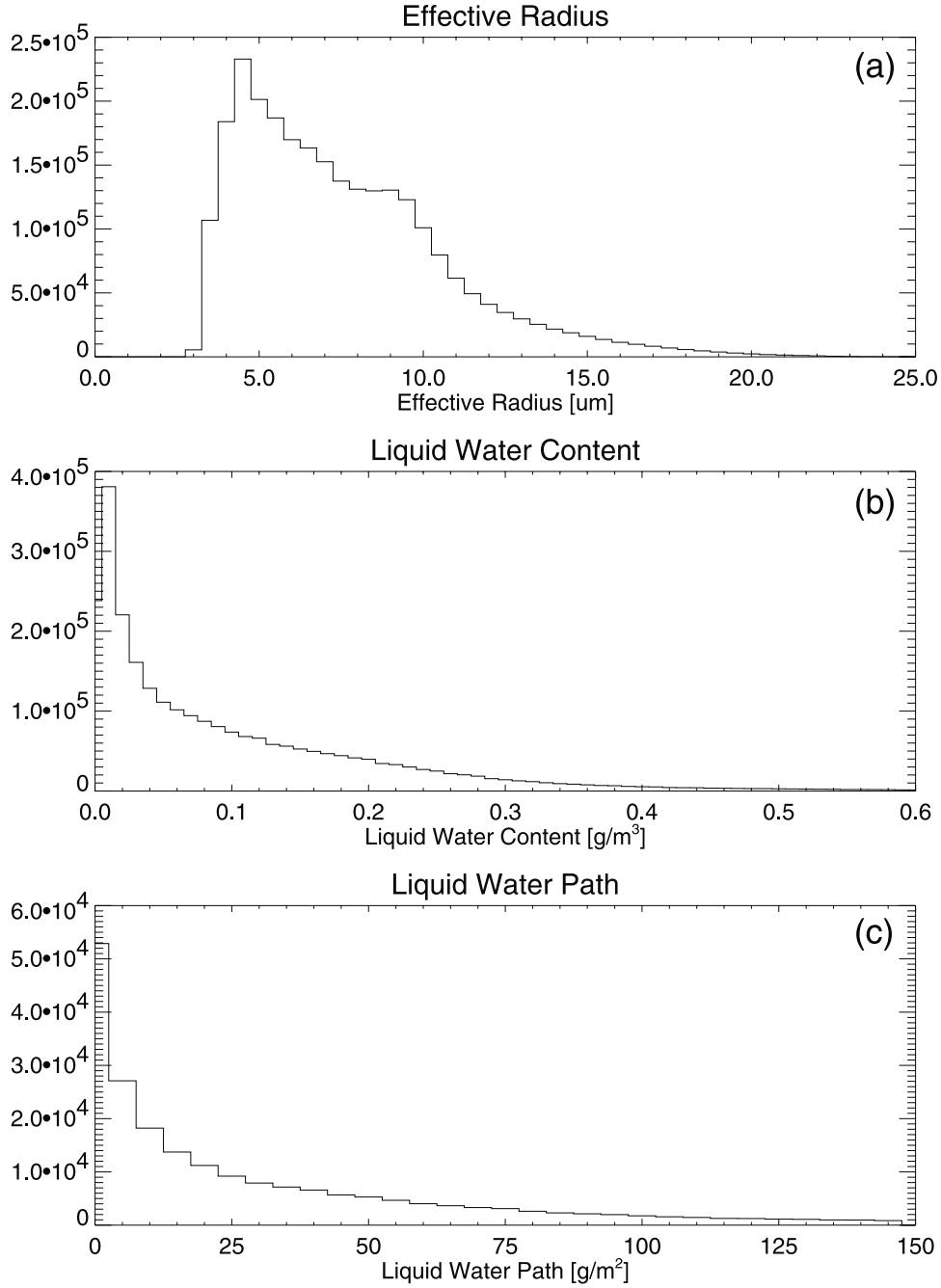


Figure 13. Histograms of retrieved (a) effective radius, (b) liquid water content, and (c) liquid water path for nonprecipitating liquid water clouds at Nauru from June to August 1999.

retrieval process) can understand the degree of certainty associated with each retrieval value.

Appendix A: Equations

[70] A 3-D Gaussian distribution, $p(x, y, z)$, is represented by nine parameters: the means and standard deviations of each variable ($\mu_x, \mu_y, \mu_z, \sigma_x, \sigma_y, \sigma_z$) and the correlations between the variables ($\rho_{xy}, \rho_{xz}, \rho_{yz}$). If one variable, z , is known, then the parameters ($\mu'_x, \mu'_y, \sigma'_x, \sigma'_y, \rho'_{xy}$) of the conditional 2-D distribution, $p(x, y|z)$ can be analytically related to the parameters of the original distribution by the following equations.

$$\mu'_x = \mu_x + \frac{\sigma_x \rho_{xz} (z - \mu_z)}{\sigma_z} \quad (\text{A1})$$

$$\sigma'_x = \sigma_x \sqrt{1 - \rho_{xz}^2} \quad (\text{A2})$$

$$\mu'_y = \mu_y + \frac{\sigma_y \rho_{yz} (z - \mu_z)}{\sigma_z} \quad (\text{A3})$$

$$\sigma'_y = \sigma_y \sqrt{1 - \rho_{yz}^2} \quad (\text{A4})$$

$$\rho'_{xy} = \frac{\rho_{xy} - \rho_{xz} \rho_{yz}}{\sqrt{(1 - \rho_{xz}^2)(1 - \rho_{yz}^2)}} \quad (\text{A5})$$

Table 4. Statistics of the Retrieved Parameters for Nonprecipitating Liquid Water Clouds at Nauru From June to August 1999

Parameter	Mean	Median	Standard Deviation
LWP, g/m ²	58.2	20.3	122.4
Optical depth	9.2	4.5	15.1
LWC, g/m ³	0.112	0.066	0.144
r_e , μm	7.82	7.17	3.18

[71] To create vertical profiles of M_2 and M_3 from a given reflectivity profile, we treat each mode of the prior pdf separately, and take the logarithm of the parameters so that we have two 3-D Gaussian distributions. Since we have no information on vertical correlation of the size distribution moments, but we know that cloud microphysical properties exhibit vertical correlation, we use the typical decorrelation length derived in section 4.2 from the cloud radar at Nauru. For each point in the Monte Carlo integration, we create two vectors of random Gaussian deviates (\mathbf{Q}_1 , \mathbf{Q}_2) which are vertically correlated in height with the given decorrelation length. For each radar range gate, i , we generate a random number that determines which mode to use, and we calculate the parameters of the conditional 2-D Gaussian distribution, $p(\log M_{2i}, \log M_{3i} | \log M_{6i})$ for that mode. Then we generate random values of $\log M_{2i}$ and $\log M_{3i}$ from the distribution according to

$$\log M_{2i} = \mu'_{M2} + Q_1(i) \sigma'_{M2} \quad (\text{A6})$$

$$\log M_{3i} = \mu'_{M3} + \sigma'_{M3} \left(Q_1(i) \rho'_{M2,M3} + Q_2(i) \sqrt{1 - \rho'^2_{M2,M3}} \right), \quad (\text{A7})$$

where μ'_{M2} , μ'_{M3} , σ'_{M2} , σ'_{M3} , $\rho'_{M2,M3}$ are the parameters of the conditional 2-D distribution.

Appendix B: Details of LES Model

[72] The dynamics model [Stevens and Bretherton, 1996] solves the anelastic Navier-Stokes equations [Ogura and Phillips, 1962] in conservative form using 5 s time steps on a domain spanning 6.4×6.4 km horizontally and 3 km vertically, which is uniformly discretized into $64 \times 64 \times 75$ grid cells. The boundary conditions are doubly periodic in the horizontal, and rigid at the top and bottom. Surface fluxes are parameterized using surface similarity. A sponge layer at the top of the model dampens trapped buoyancy waves at altitudes >500 m above the trade inversion, which is defined as the height of the horizontally averaged surface of the 6.5 g/kg total water mixing ratio. First-order turbulence closure is used for subgrid-scale mixing [Smagorinsky, 1963; Lilly, 1962] with a stability-dependent mixing length [Deardorff, 1980] modified to account for the effects of evaporation [Mason and MacVean, 1990]. Large-scale subsidence is calculated as the product of altitude and a fixed divergence rate of $4.3 \times 10^{-6} \text{s}^{-1}$.

[73] To simulate maritime trade-wind cumulus, we adapt an idealization from Stevens *et al.* [2001] of measurements averaged over the first 5 days of the Atlantic Trade-Wind Experiment (ATEX). The model is idealized with surface

conditions, and soundings from the upstream ship in the ATEX flotilla. The sea surface temperature is fixed at 298 K, surface pressure is fixed at 1015 mbar, latitude fixed at 15° , geostrophic (and initial) winds from Figure 4 of Augstein *et al.* [1973] and soundings of temperature and water vapor mixing ratio averaged from the ATEX measurements by B. Albrecht to preserve the jumps at the base and top of the transition layer. Pseudorandom perturbations of temperature and water vapor mixing ratio are imposed below the inversion to promote turbulence initially; the amplitude of the perturbations (which horizontally average to zero) are 0.1 K and 0.025 g/kg, respectively.

[74] Large-scale advective forcings are parameterized to represent the net influx of cooler, drier air in the equatorward flow through the model domain. Following Stevens *et al.* [2001], we parameterize these forcings to fade linearly from a maximum at the surface to zero at the trade inversion. The surface drying tendency we use (1.3 g/kg/d) is taken directly from Stevens *et al.* [2001]. We double the surface cooling tendency to 2 K/d, which compensates for a clear sky cooling rate that is half the value imposed by Stevens *et al.* [2001].

[75] The aerosol and cloud microphysics model has been adapted from the 1-D implementation of Ackerman *et al.* [1995]. Here the size distributions are resolved into 20 bins over a range from 0.05 to 20 μm radius for dry condensation nuclei (CN, assumed to consist of ammonium bisulfate) and from 1 to 770 μm for cloud droplets. Within each droplet size bin the model also tracks the dissolved CN. The microphysics model treats the processes of droplet nucleation, condensation, evaporation, and coalescence (between droplets only), as described in detail by Ackerman *et al.* [1995]. The dynamics model treats the transport (including sedimentation) of all microphysics fields, and the microphysics model is called once per dynamic time step to adjust the model variables for changes due to microphysical processes. As done by Kogan [1991], the dynamical forcing of supersaturation is uniformly spread over a number of substeps. Instead of using a fixed number of substeps, we choose a substep duration separately at each grid point such that the Courant number for condensation in the smallest

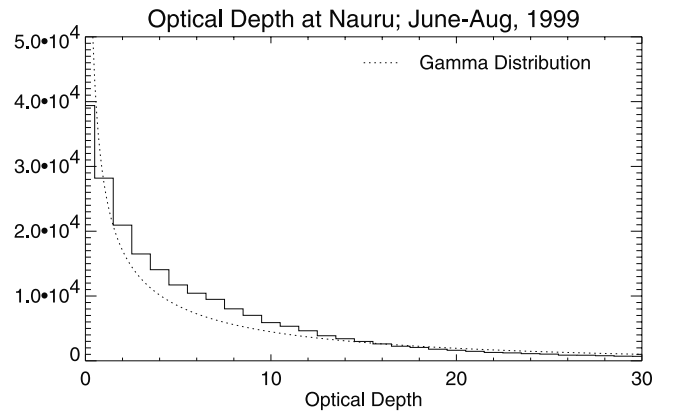


Figure 14. Histogram of retrieved liquid water path for nonprecipitating liquid water clouds at Nauru from June to August 1999. A gamma distribution (dotted line) whose parameters are given in the text is also shown.

bin with droplet concentrations $>0.1 \text{ cm}^{-3}$; the smallest substep (0.1 s) is taken when the dynamically forced supersaturation will cross zero or nucleation of droplet will exceed 1 cm^{-3} .

[76] The model domain is initially cloud free. For case 1, we initialize a spatially uniform, lognormal distribution of CN with a number concentration of 250 cm^{-3} , and a geometric mean radius and standard deviation of $0.1 \mu\text{m}$ and 1.2. The total particle number concentration at each grid point is fixed by diagnosing the CN distribution from the droplet number concentration and the initial CN distribution after every substep. For case 2, the initial CN distribution has a number concentration of 150 cm^{-3} .

[77] Radiative transfer is calculated for each column once every minute during the simulation using a two-stream model [Toon *et al.*, 1989] in which water vapor continuum absorption has been modified [Clough *et al.*, 1989]. By treating longwave radiation only, we are effectively simulating nocturnal conditions. Aerosol and cloud optical properties are computed through Mie calculations using the complex index of refraction for liquid water compiled by Ackerman *et al.* [1995]. We specify the emissivity of the sea surface to be unity, and fix the overlying water vapor column at 1 g/cm^2 .

[78] **Acknowledgments.** We would like to thank Sonia Lasher-Trapp for her help with the SCMS data and Eugene Clothiaux for answering our many queries about the ARSCL data product. This research was supported by the Office of Biological and Environment Research of the U.S. Department of Energy (under grant DE-A1005-90ER61069 to the NASA Goddard Space Flight Center) as part of the Atmospheric Radiation Measurement Program. S. McFarlane was supported in part by a National Science Foundation Graduate Research Fellowship.

References

- Ackerman, A. S., O. B. Toon, and P. Hobbs, A model for particle microphysics, turbulent mixing, and radiative transfer in the stratocumulus-topped boundary layer and comparisons with measurements, *J. Atmos. Sci.*, 52, 1204–1236, 1995.
- Augstein, E., H. Riehl, F. Ostapoff, and V. Wagner, Mass and energy transports in an undisturbed Atlantic trade-wind flow, *Mon. Weather Rev.*, 101, 101–111, 1973.
- Barker, H. W., A parameterization for computing grid-averaged solar fluxes for inhomogeneous marine boundary layer clouds, part I, Methodology and homogeneous biases, *J. Atmos. Sci.*, 53, 2289–2303, 1996.
- Barker, H. W., B. A. Wielicki, and L. Parker, A parameterization for computing grid-averaged solar fluxes for inhomogeneous marine boundary layer clouds, part II, Validation using satellite data, *J. Atmos. Sci.*, 53, 2304–2316, 1996.
- Baumgardner, D., Airborne measurements for cloud microphysics, *Bull.* 24, NCAR Res. Aviation Facil., Boulder, Colo., 1989.
- Bernardo, J., and A. Smith, *Bayesian Theory*, John Wiley, New York, 1994.
- Clothiaux, E. E., K. P. Moran, B. E. Martner, T. P. Ackerman, G. G. Mace, T. Uttal, J. H. Mather, K. B. Widener, M. A. Miller, and D. J. Rodriguez, The Atmospheric Radiation Measurement Program cloud radars: Operational modes, *J. Atmos. Oceanic Technol.*, 16, 819–827, 1999.
- Clothiaux, E. E., T. P. Ackerman, G. G. Mace, K. P. Moran, R. T. Marchand, M. A. Miller, and B. E. Martner, Objective determination of cloud heights and radar reflectivities using a combination of active remote sensors at the ARM CART sites, *J. Appl. Meteorol.*, 39, 645–665, 2000.
- Clough, S. A., F. X. Kneizys, and R. W. Davies, Line shape and the water vapor continuum, *Atmos. Res.*, 23, 229–241, 1989.
- Deardorff, J. W., Stratocumulus-capped mixed layers derived from a three-dimensional model, *Boundary Layer Meteorol.*, 18, 495–527, 1980.
- Dong, X., T. P. Ackerman, E. E. Clothiaux, P. Pilewskie, and Y. Han, Microphysical and radiative properties of boundary layer stratiform clouds deduced from ground-based measurements, *J. Geophys. Res.*, 102, 23,829–23,843, 1997.
- Evans, K. F., S. J. Walter, A. J. Heymsfield, and G. M. McFarquhar, Submillimeter-Wave Cloud Ice Radiometer: Simulations of retrieval algorithm performance, *J. Geophys. Res.*, 107(3), 10.1029/2001JD000709, 2002.
- Fox, N. I., and A. J. Illingworth, The retrieval of stratocumulus cloud properties by ground-based cloud radar, *J. Appl. Meteorol.*, 36, 485–492, 1997.
- French, J. R., G. Vali, and R. D. Kelly, Observations of microphysics pertaining to the development of drizzle in warm, shallow cumulus clouds, *Q. J. R. Meteorol. Soc.*, 126, 415–443, 2000.
- Frisch, A. S., C. W. Fairall, and J. B. Snider, Measurement of stratus cloud and drizzle parameters in ASTEX with a Ka-band Doppler radar and a microwave radiometer, *J. Atmos. Sci.*, 52, 2788–2799, 1995.
- Frisch, A. S., G. Feingold, C. W. Fairall, T. Uttal, and J. B. Snider, On cloud radar and microwave radiometer measurements of stratus cloud liquid water profiles, *J. Geophys. Res.*, 103, 23,195–23,197, 1998.
- Han, Y., and E. R. Westwater, Analysis and improvement of tipping calibration for ground-based microwave radiometers, *IEEE Trans. Geosci. Remote Sens.*, 38, 1–18, 2000.
- Kogan, Y. L., The simulation of a convective cloud in a 3-D model with explicit microphysics, part I, Model description and sensitivity experiments, *J. Atmos. Sci.*, 48, 1160–1189, 1991.
- Lhermitte, R., Attenuation and scattering of millimeter wavelength radiation by clouds and precipitation, *J. Atmos. Oceanic Technol.*, 7, 464–479, 1990.
- Liao, L., and K. Sassen, Investigation of relationships between Ka-band radar reflectivity and ice and liquid water contents, *Atmos. Res.*, 34, 231–248, 1994.
- Liljegren, J., Combining microwave radiometer and millimeter cloud radar to improve integrated liquid water retrievals, paper presented at Ninth Atmospheric Radiation Measurement Program Science Team Meeting, Atmos. Radiat. Meet., San Antonio, Tex., 1999.
- Lilly, D. K., On the numerical simulation of buoyant convection, *Tellus*, 14, 101–171, 1962.
- Mace, G. G., and K. Sassen, A constrained algorithm for retrieval of stratocumulus cloud properties using solar radiation, microwave radiometer, and millimeter cloud radar data, *J. Geophys. Res.*, 105, 29,099–29,108, 2000.
- Mason, P. J., and M. K. MacVean, Cloud-top entrainment instability through small-scale mixing and its parameterization in numerical models, *J. Atmos. Sci.*, 47, 1012–1030, 1990.
- Miles, N. L., J. Verlinde, and E. E. Clothiaux, Cloud droplet size distributions in low-level stratiform clouds, *J. Atmos. Sci.*, 57, 295–311, 2000.
- Miller, E. R., J. Wang, and H. L. Cole, Correction for dry bias in vaisala radiosonde rh data, paper presented at Ninth Annual Atmospheric Radiation Measurement Science Team Meeting, Atmos. Radiat. Meet., San Antonio, Tex., 1999.
- Moran, K. P., B. E. Martner, D. Welsh, D. Merritt, M. Post, and T. Uttal, ARM's cloud profiling radar, paper presented at 28th Conference on Radar Meteorology, Am. Meteorol. Soc., Austin, Tex., 1997.
- Moran, K. P., B. E. Martner, M. J. Post, R. A. Kropfli, D. C. Welsh, and K. B. Widener, An unattended cloud-profiling radar for use in climate research, *Bull. Am. Meteorol. Soc.*, 79, 443–455, 1998.
- Ogura, Y., and N. Phillips, Scale analysis of deep and shallow convection in the atmosphere, *J. Atmos. Sci.*, 19, 173–179, 1962.
- Oreopoulos, L., and H. W. Barker, Accounting for subgrid-scale cloud variability in a multi-layer 1D solar radiative transfer algorithm, *Q. J. R. Meteorol. Soc.*, 125, 301–330, 1999.
- Raga, G. B., J. B. Jensen, and M. B. Baker, Characteristics of cumulus band clouds off the coast of Hawaii, *J. Atmos. Sci.*, 47, 338–355, 1990.
- Rodgers, C. D., *Inverse Methods for Atmospheric Sounding: Theory and Practice*, World Sci., River Edge, N. J., 2000.
- Rosenkranz, P. W., Water vapor microwave continuum absorption: A comparison of measurements and models, *Radio Sci.*, 33, 919–928, 1998.
- Sassen, K., G. G. Mace, Z. Wang, M. R. Poellot, S. M. Sekelsky, and R. E. McIntosh, Continental stratus clouds: A case study using coordinated remote sensing and aircraft measurements, *J. Atmos. Sci.*, 56, 2345–2358, 1999.
- Sivia, D. S., *Data Analysis: A Bayesian Tutorial*, Oxford Univ. Press, New York, 1996.
- Smagorinsky, J., General circulation experiments with the primitive equations, 1, The basic experiment, *Mon. Weather Rev.*, 91, 99–164, 1963.
- Stevens, D. E., and C. S. Bretherton, A forward-in-time advection scheme and adaptive multilevel flow solver for nearly incompressible flow, *J. Comput. Phys.*, 129, 284–289, 1996.

- Stevens, B., et al., Trade-wind cumuli under a strong inversion, *J. Atmos. Sci.*, 58, 1870–1891, 2001.
- Toon, O. B., C. P. McKay, and T. P. Ackerman, Rapid calculation of radiative heating rates and photodissociation rates in inhomogeneous multiple scattering atmospheres, *J. Geophys. Res.*, 94, 16,287–16,301, 1989.
- Westwater, E. R., Accuracy of water vapor and cloud liquid determination by dual-frequency, ground-based microwave radiometry, *Radio Sci.*, 13, 677–685, 1978.
- Westwater, E., Y. Han, B. B. Stankov, B. M. Lesht, C. N. Long, and J. Shannahoff, Microwave radiometers and radiosondes during Nauru99, paper presented at Proceedings of Tenth Atmospheric Radiation Measurement Science Team Meeting, Atmos. Radiat. Meet., San Antonio, Tex., 2000.
-
- A. S. Ackerman, NASA Ames Research Center, Room 240 Building 245, Mail Stop 245-4, Moffett Field, CA 94035-1000, USA. (ack@sky.arc.nasa.gov)
- K. F. Evans and S. A. McFarlane, Program in Atmospheric and Oceanic Sciences, University of Colorado at Boulder, Campus Box 311, Boulder, CO 80309-0311, USA. (evans@nit.colorado.edu; mcfarlan@candela.colorado.edu)

Bayesian Retrievals - Nauru 6/05/99

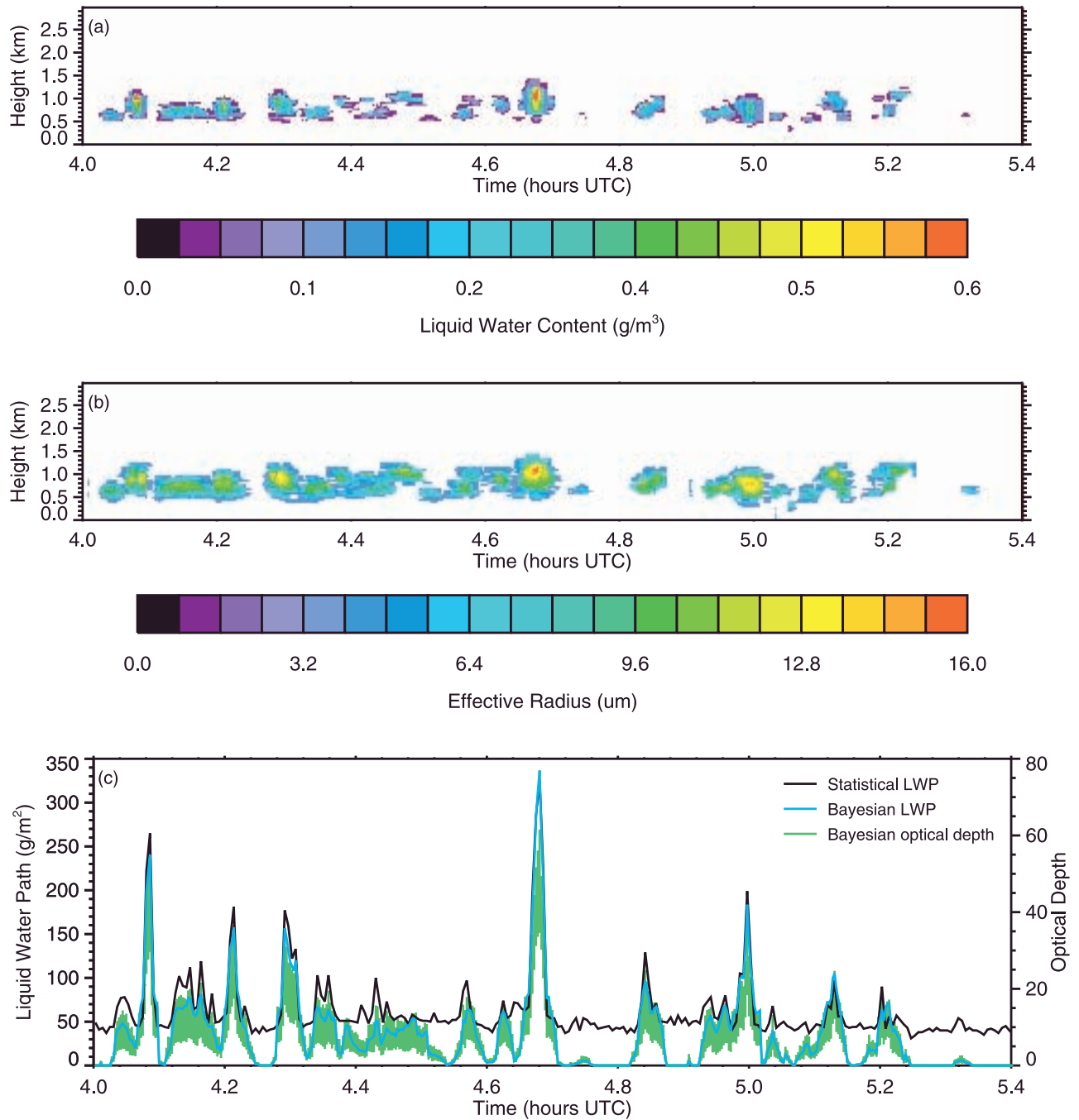


Figure 12. Examples of Bayesian retrievals at Nauru on 5 June 1999. Time–height cross sections of (a) retrieved liquid water content and (b) effective radius. (c) Time series of retrieved liquid water path and optical depth at Nauru. The black line is the ARM retrieved statistical liquid water path during this time. The blue line is the Bayesian retrieved liquid water path, and the green line is the Bayesian optical depth plus error bars.